Regional Studies in Marine Science 58 (2023) 102797

Contents lists available at ScienceDirect

Regional Studies in Marine Science

journal homepage: www.elsevier.com/locate/rsma

Development of Ag-doped on multi-walled carbon nanotubes for the treatment of fish pond effluent

Saadatu Aliyu [a,d], Abdulkareem Saka Ambali [b,d], Tijani Jimoh Oladejo [c,d], Saheed Mustapha [c,d,*], Titus Chinedu Egbosiuba [e], Samson Oluwaseyi Bada [f]

[a] Niger State College of Agriculture, PMB 109, Mokwa, Niger State, Minna, Nigeria
[b] Department of Chemical Engineering, Federal University of Technology, PMB 65, Minna, Niger State, Nigeria
[c] Department of Chemistry, Federal University of Technology, PMB 65, Minna, Niger State, Nigeria
[d] Nanotechnology Research Group, African Centre of Excellence on Mycotoxin and Food Safety (ACEMFS), Federal University of Technology, PMB 65, Bosso, Minna, Niger State, Nigeria
[e] Department of Chemical Engineering, Chukwuemeka Odumegwu Ojukwu University, PMB 02, Uli, Anambra State, Nigeria
[f] DSI-NRF SARChI Clean Coal Technology Research Group, School of Chemical and Metallurgical Engineering, Faculty of Engineering and the Built Environment, University of the Witwatersrand, Wits 2050, Johannesburg, South Africa

ARTICLE INFO

Article history:
Received 17 June 2022
Received in revised form 10 December 2022
Accepted 16 December 2022
Available online 21 December 2022

Keywords:
Silver nanoparticles
Carbon nanotubes
Nanoadsorbents
Adsorption
Fish pond wastewater

ABSTRACT

The treatment of fish pond wastewater utilizing nanocomposites by batch adsorption using purified carbon nanotubes and silver-doped carbon nanotubes (CNTs) as nano-adsorbents was explored in this study. Ultraviolet spectroscopy, X-ray diffraction (XRD), and high-resolution transmission electron microscopy (HRTEM) were used to confirm the biosynthesized AgNPs. The metallic silver is associated with the peaks in the XRD pattern, and HRTEM studies indicated that AgNPs are between particle sizes of 11.12 and 15.39 nm. Purified carbon nanotubes (P-CNTs) and silver-doped carbon nanotubes (Ag-CNTs) were produced using a Fe–Ni/kaolin catalyst in a catalytic chemical vapour deposition process, followed by acid purification and doped with silver nanoparticles, respectively. HRTEM, HRSEM, FTIR, and BET were used to characterize the as-synthesized CNTs, P-CNTs, and Ag-CNTs. Both unpurified and purified CNTs were tube-like, extremely porous, and crystalline, with Ag-CNTs having a higher surface area (1068 m^2/g) greater than P-CNTs (268.40 m^2/g). The batch adsorption process was used to investigate the adsorption behaviour of P-CNTs and Ag-CNTs to remove Fe, Mn, and Zn from fish pond effluent as a function of contact time, adsorbent dosage, and temperature. The Freundlich isotherm described equilibrium sorption data better than the Langmuir isotherm, and the adsorption kinetics fit well with the pseudo-second-order model. A thermodynamic study of the adsorption process found that the change in Gibbs free energy was negative, indicating that the adsorption process was feasible and spontaneous. Consequently, it has been demonstrated that removing heavy metals from aquatic effluent using Ag-doped CNTs is effective in aquaculture.

1. Introduction

Human activities from domestic, industrial, commercial, or agricultural use, surface runoff or stormwater, and sewer intake or infiltration were sources of wastewater (Luo et al., 2014). High quantities of nutrients and solid debris which characterize these wastewaters are typically dumped into the water bodies, resulting in pollution and environmental and health risks. Aquatic feeds contain extremely nutritious and chemical products, which have resulted in waste that is difficult to control and dangerous to aquatic life. Aquaculture wastes are primarily made up of nitrogenous wastes, which are highly poisonous to macrofauna in open bodies of water. These issues and the rapid expansion of fish farming demanded the implementation of controls for fish farm effluent and wastewater (Anijiofor et al., 2018). Physical factors such as pH, total suspended solids (TSS), total dissolved solids (TDS), ammonia, turbidity and colour, and organic contaminants are some metrics of fish effluent that affect the aquatic environment. The increase in ammonia concentrations could raise blood ammonia levels, making it very harmful to fish, similar to suspended particles, which cause interstitial clogging and substrate embedment in fish (Omitoyin et al., 2017).

The level of pollution caused to the fish and fish pond is determined by water sources, water scarcity, and the nature of additives employed in fish farming. Growing environmental awareness and stricter regulatory standards have prompted

* Corresponding author at: Department of Chemistry, Federal University of Technology, PMB 65, Minna, Niger State, Nigeria.
E-mail address: saheedmustapha09@gmail.com (S. Mustapha).

https://doi.org/10.1016/j.rsma.2022.102797
2352-4855/

numerous industries to find adequate wastewater treatment methods (Teh et al., 2016). As a result, it is critical to treat wastewater from fish ponds for reuse and safeguard the environment surrounding fish farms. Existing wastewater treatment technologies, such as sedimentation, flocculation, disinfection, filtration, ozonation, and UV (ultraviolet) light, have various disadvantages, such as high energy consumption and insufficient pollutant removal, and toxic sludge production. Thus, finding effective and reliable solutions for treating municipal and industrial wastewater is critical. Among the different new technologies, nanotechnology via adsorption deemed an attractive technique has enormous potential for wastewater treatment due to its advantages, such as high flexibility, simplicity of design, ease of operation, insensitivity to toxic pollutants, and small concentrations of harmful compounds. Various efficient, eco-friendly, and cost-effective nanomaterials like carbon nanotubes (CNTs), metallic nanoparticles, graphene, and zeolite with distinct capabilities for successful wastewater decontamination.

CNTs are carbon compounds made up of rolled-up graphene layers in tubes. Single-walled CNTs (SWCNTs) are made up of only one layer of tube, whereas multi-walled CNTs (MWCNTs) are made up of many layers of tube. Arc discharge, laser ablation, electrolysis, flame synthesis, and catalytic chemical vapour deposition (CCVD) are techniques used to produce CNTs. Because of its capacity to control growth directions and scale-up manufacturing in large quantities, the CCVD process is most extensively employed (Alfarisa et al., 2016). Multi-walled carbon nanotubes (MWCNTs) have been widely used as a new adsorbent for removing various organic and inorganic contaminants from wastewater because of their enormous specific surface area, high aspect ratio, and layered structures (Hamzat et al., 2019). Despite these positive attributes, carbonaceous material aggregation during and after synthesis impacts and limits CNTs efficiency. As a result, it is necessary to change the surface of pure CNTs to improve their adsorption capacity and dispersion rate (Lu et al., 2008).

Metallic nanoparticles such as silver nanoparticles (AgNPs) have attracted a lot of interest due to their antibacterial and adsorptive properties (Farid et al., 2018). Silver nanoparticles are synthesized using green nanoparticle synthesis, which is environmentally beneficial. *Xanthium strumerium* (Rough cocklebur), *Murrayakoenigii* (curry), *Ocimum sanctum* (Tulsi), *Acacia farnesiana* (Acacia), *Macrotyloma uniflorum* (Horsegram), and even fruit extracts of *Musa paradisiacal* (banana peels) have all been used to synthesize AgNPs with significant antimicrobial activity. These plant extracts act as reducing and/or capping agent in the reaction with silver nitrate when synthesizing AgNPs. Therefore, the antibacterial efficacy, biocompatibility, and depollution efficiency of produced AgNPs could be improved by doping them onto the matrix CNTs. For example, Goscianska and Pietrzak (2015) coated MWCNTs with silver nanoparticles to remove the anionic tartrazine colour from an aqueous solution. The azo dye adsorption capability of multi-walled carbon nanotubes increased as silver nanoparticles increased. Carbon nanotubes treated with silver nanoparticles have lower adsorption capabilities in the following order: CNTs (52.24 mg/g) > 5 Ag/CNTs (84.04 mg/g) > 3 Ag/CNTs (72.33 mg/g) > 1 Ag/CNTs (62.07 mg/g) > 5 Ag/CNTs (84.04 mg/g) > 5 Ag/CNTs (72.33 mg/g). These experiments show that varied loading concentrations of AgNPs on the surface of CNTs can be a promising material for water treatment. Ag/N-doped TiO_2/CNT was used to remove formaldehyde under visible light irradiation, and they found the materials to be sufficient in environmental purification systems (Tan et al., 2022). Khalatbary et al. (2022) used γ-Fe_2O_3/MWCNTs/Ag nanocomposites to remove sulphamethazine from an aqueous solution. They reported that the exothermic nature of the adsorption process obeyed the pseudo-second-order model, and the reusability result showed the potential removal efficiency of the pollutant even after four adsorption cycles. In the studies of Kai et al. (2022) and Yang et al. (2022), *R. palustris*/CNTs/Ag/TiO_2 and CNTs/Ag/TiO_2 were used for the degradation and mineralization of dye wastewater. However, little or no knowledge of investigating the adsorptive removal of some toxic metals from fish pond wastewater using AgNPs/CNTs composite and its promising approach for useability has been investigated.

In this study, the production and characterization of MWCNTs using the CCVD method with Fe–Ni/kaolin as the catalyst and green synthesis of silver nanoparticles using an extract from *Carica papaya* leaves as a reducing and stabilizing agent doped on the MWCNTs through a wet impregnation method are investigated. Some physicochemical parameters of fish pond wastewater before and after treatment with pure-CNTs and AgNPs using adsorption studies are presented. In addition, the isotherm, kinetic, thermodynamic, and regeneration of nanomaterials for their potential uses in wastewater were also performed.

2. Materials and methods

The reagents such as iron(III) trioxonitrate (V) nonahydrate [$Fe(NO_3)_3.9H_2O$, 99.95%], nickel(II) trioxonitrate (V) hexahydrate [$Ni(NO_3)_2.6H_2O$, 99.99%], silver trioxonitrate (V) ($AgNO_3$, 99.99%), nitric acid (HNO_3, 65%) and sulphuric acid (H_2SO_4, 98%) were purchased from Sigma-Aldrich. All the reagents used without further purification in this study were of analytical grade. The kaolin used as catalyst support was collected from Kankara in Kastina State, Nigeria. All of the chemicals and gases used are of the highest quality. A catalytic chemical vapour deposition (CCVD) approach was used to synthesize carbon nanotubes (CNTs). CNTs were produced in this study by decomposing acetylene (C_2H_2) over the synthesized Fe–Ni/kaolin catalyst using the wet impregnation method.

2.1. Preparation of Fe–Ni/Kaolin catalyst

Utilizing the wet impregnation process, the catalyst was prepared. 4.04 g $Fe(NO_3)_3.9H_2O$ and 2.91 g $Ni(NO_3)_2.6H_2O$ were weighed in a beaker and dissolved in 50 cm^3 de-ionized water. The 8 g of kaolin support was added to the mixture and agitated on a magnetic stirrer for 30 min at 120 rpm. The resultant mixture was then oven-dried for 8 h at 120 °C, cooled to room temperature, ground, and screened through a 150 μm sieve, as shown in Plate 1 (A and B). The nitrates were decomposed by the catalyst powders after being calcined at 500 °C for 16 h in a furnace. The sample was weighed and recorded to determine the yield using Eqs. (1) and (2).

$$\text{Catalyst yield before calcination} = \frac{\text{weight before oven drying} - \text{weight after oven drying}}{\text{weight before oven drying}} \times 100 \quad (1)$$

$$\text{Catalyst yield after calcination} = \frac{\text{weight before calcination} - \text{weight after calcination}}{\text{weight before calcination}} \times 100 \quad (2)$$

2.2. Carbon nanotube synthesis

As depicted in Plate 1(C), CNTs were produced by decomposing the carbon source (acetylene) in a tubular quartz reactor positioned horizontally in a furnace. The heating rate of the furnace, reaction temperature, and gas flow rates are precisely regulated as needed, thanks to electronic control. In the center

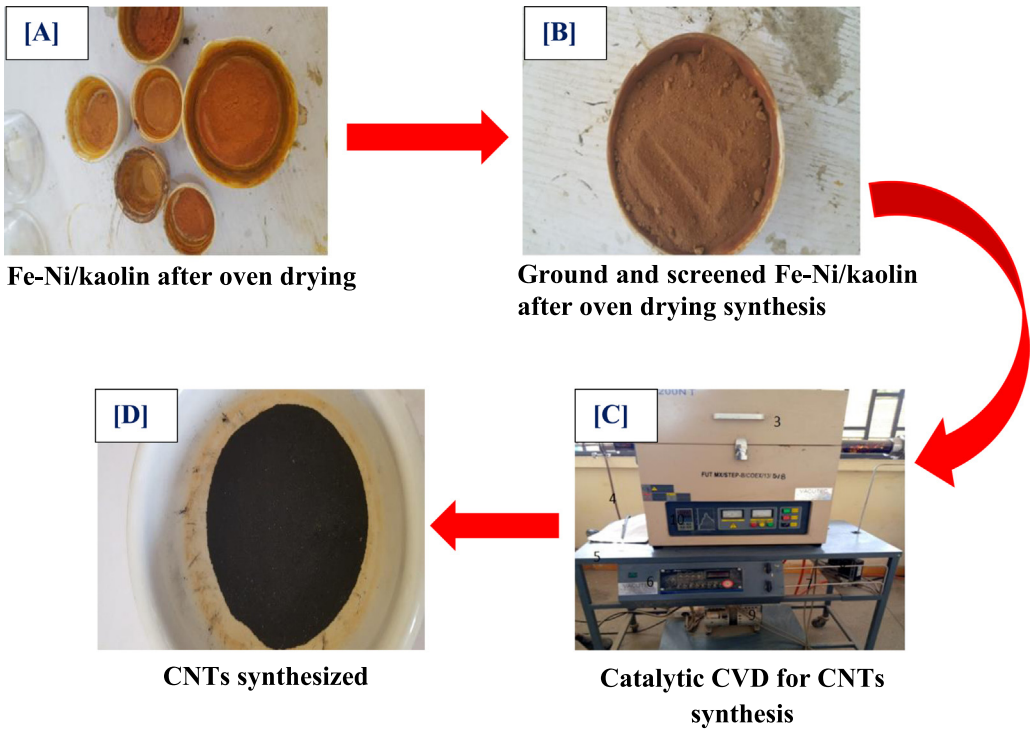

Plate 1. A flow diagram for the synthesis of CNTs.

of the quartz tube, the catalyst, 1.0 g, was positioned in a quartz boat, with the catalyst spread out into a thin layer. To establish an inert environment, remove the impurity, and stop the samples from oxidizing before and after the reaction period, the furnace was heated at 10 °C/min while argon was flowing into the system at 30 mL/min. The argon flow rate was set to 230 mL/min once the temperature reached the designated reaction temperature of 750 °C, and C_2H_2 was injected at a flow rate of 150 mL/min to begin the onset of CNTs growth. After the 45-min setup reaction period, the C_2H_2 flow was discontinued, and the furnace was allowed to cool to ambient temperature on a continuous flow of argon for 30 ml/min. The boat was taken out of the reactor and the produced CNTs, as seen in Plate 1(D), were weighed and recorded. Using the relationship indicated in Eq. (3), the CNTs yield (%) was calculated.

$$\text{CNTs yield } (\%) = \frac{\text{Weight product} - \text{Weight catalyst}}{\text{Weight catalyst}} \times 100 \quad (3)$$

2.2.1. Purification of the as-synthesized CNTs

The raw CNTs (see Plate 1D) were purified using the acid treatment. 5 g of the synthesized CNTs were combined with 300 cm^3 of mixed acids (HNO_3 and H_2SO_4 at v/v 1:3) in an ultrasonic bath and then sonicated at 40 °C for 90 min. This was done to remove any remaining Fe, Ni, amorphous carbon, or support material (kaolin) from the CNTs when they were produced and to provide oxygen on the surface of the material. The pH of 7 was achieved by cooling the CNTs to room temperature, washing them repeatedly with de-ionized water, and filtering them. The wet purified CNTs (P-CNTs) is dried in an oven at 120 °C for 12 h.

2.3. Synthesis of silver nanoparticles (AgNPs)

Carica papaya leaves were washed thoroughly with de-ionized water and sun-dried to air dry to remove any remaining moisture. 10 g powdered leaves were combined with 100 cm^3 of de-ionized water and heated at 60 °C for 30 min. After the solution turned light yellow, it was cooled to room temperature, filtered through Whatman filter No. 1, and kept in a refrigerator at 4 °C.

In the biosynthesis of AgNPs, silver nitrate aqueous solution (1 mM) was prepared by weighing 0.16987 g of the silver nitrate crystals using a weighing balance and dissolved in 100 cm^3 of de-ionized water (10 mM stock of $AgNO_3$). The obtained silver nitrate solution was kept in a brown reagent bottle and used to synthesize silver nanoparticles. 5 cm^3 of aqueous extract of pawpaw leaves (as seen in Plate 2(a)) was added to 95 cm^3 of an aqueous solution of 1.0 mM $AgNO_3$ and heated on a magnetic stirrer at 60 °C for 30 min. The brown colour formation indicated the synthesis of silver nanoparticles (Plate 2(b)), which were cooled to room temperature and transferred to an opaque brown bottle. The obtained AgNP was characterized using a UV–Vis spectroscopy.

2.4. Preparation of silver-doped multi-walled carbon nanotubes (Ag-CNTs)

The adopted method for the preparation of Ag-CNTs followed the previously reported procedure for the synthesis of AgNPs. Different volumes of 20, 40, 60, 80, and 100 cm^3 AgNP solutions each were added to 0.1 g of P-CNTs, and the resultant mixtures were first centrifuged for 10 min after being sonicated for 18 h at 60 °C. After centrifugation, de-ionized water was used to wash the black solid residue until it achieved a pH of 7 and oven-dried at 105 °C for 12 h. To characterize the Ag-CNTs, they were oven-dried.

2.5. Characterization of synthesized nanomaterials

The support material (kaolin), synthesized catalyst, as-prepared CNTs, purified CNTs, AgNPs, and Ag-CNTs were characterized using different analytical tools. The XRF and BET were used as the main characterization technique for the support material (kaolin) to determine the elemental composition and surface area of kaolin, respectively. The BET, FTIR, XRD, EDX/HRSEM,

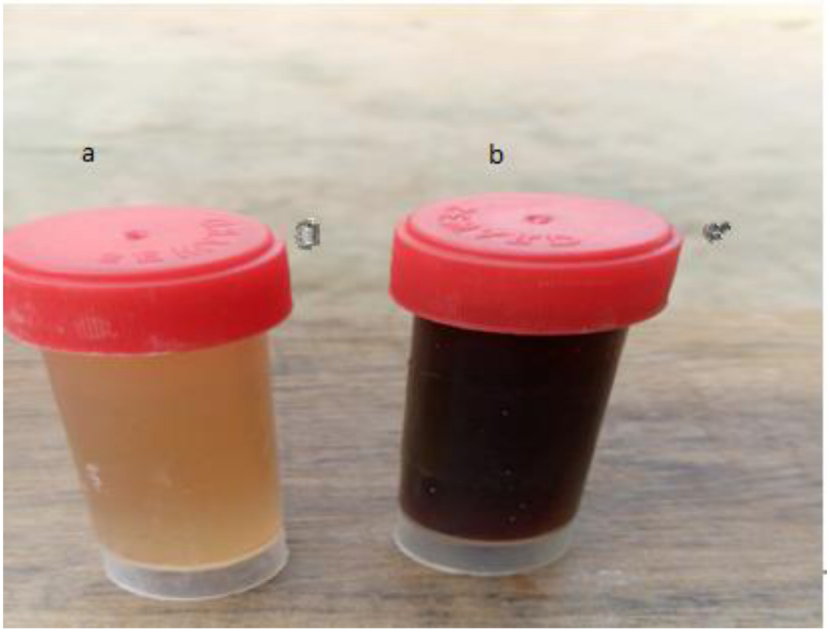

Plate 2. (a) Aqueous extract of pawpaw leaves (b) AgNPs from pawpaw leaf extract.

and SAED/HRTEM were techniques used to determine the quality of the catalyst (Fe–Ni/kaolin catalyst). While TGA, BET, XRD, EDX/HRSEM, SAED/HRTEM, and XPS were used to characterize the unpurified and purified CNTs, AgNPs and Ag-CNTs.

The X-ray fluorescence Philips PW2400 analyser was used to determine the elemental composition of the kaolin sample. Exactly 300 mg of kaolin sample was prepared by pressing it into cellulose before analysing it on a Philips PW2400 XRF spectrometer using calibration software designed from standard reference materials to determine its elemental composition. The thermal stabilities of the samples were examined using a thermalgravimetric Perkin Elmer STA 4000 analyser. Samples with a known weight (15 mg) were placed in a ceramic pan and heated from room temperature to 900 °C at a rate of 10 °C/min while being exposed to nitrogen gas at a pressure of 2.5 bar and a flow rate of 20 mL/min. The NOVA 4200e Quantachrome instrument analyser was used to analyse the BET surface area and total pore volume. 300 mg samples were degassed at 150 °C for 4 h under a nitrogen gas flow to eliminate contaminants and water moisture. The adsorbate used was nitrogen gas. At -196 °C, the surface areas and pore size distributions were then measured. Using nitrogen adsorption/desorption, the BET method was used to determine the pore size distribution of the samples for certain surface areas.

The structural to functional alterations in the sample were examined using a Fourier transforms infrared (FTIR) spectrometer. A Perkin Elmer Frontier FTIR spectrometer was used for this analysis. The FTIR spectra were captured at a resolution of 400 to 4400 cm^{-1} and a scan speed of 0.125 cm/s. Using a Bruker AXS D8 Advance X-ray diffractometer with Cu K radiation, XRD patterns were captured from Bragg's angles of 10 to 90°. The elemental composition was ascertained by combining the HRSEM with energy-dispersive X-ray spectroscopy (EDX). Zeiss Auriga with electron high tension at 5 kV was used for this investigation. The Zeiss Auriga model was used to carry out HRTEM and selected area electron diffraction (SAED). The non-monochromatic MgK X-ray source (1253.6 eV, 15 kV, 200 W) and hemispherical sector analyser were used in the XPS analyses, which were conducted with a PHI 5400 XPS spectrometer. The spectrometer dispersion was adjusted to offer binding energy (BE) of 932.67 eV for the Cu 2p3/2 line of metallic copper, and the instrument work function was calibrated to give a BE of 83.96 eV for the Au 4f7/2 line of metallic gold.

2.6. Characterization of fish pond wastewater

The wastewater from the fish pond was collected from FAIB Construction International in Minna, Niger State, Nigeria. The physicochemical properties of the wastewater were measured using the methods described by American Public Health Association (American Public Health Association , APHA). A pH meter was used to calculate the pH of the effluent. Similarly, the dissolved oxygen level (DO) was determined using the DO meter, and the pH and electrical conductivity were calculated using a multiparameter analyser C 3010. The standard methods outlined by the American Public Health Association (APHA) were used to determine the following chemical parameters: chemical oxygen demand (COD), biochemical oxygen demand (BOD), total dissolved solids (TDS) alkalinity, and the total amount of nitrate, sulphate, phosphate, ammonium, chloride, magnesium, potassium, and calcium. The atomic absorption spectrophotometer (AAS) (Perkin Elmer 200) was used to measure the concentration of heavy metals in the fish pond wastewater before and after treatment. Eq. (4) was used to compute the quantity of metal adsorbed (Mustapha et al., 2019).

$$Q = \frac{(C_o - C_e)V}{M} \tag{4}$$

where C_o is the initial concentration of the metal in the fishpond wastewater before adsorption in mg/L, C_e is the concentration of a metal ion in the filtrate after adsorption in mg/L, M is the weight of the adsorbent (mg), V is the volume of adsorbate (L), and Q is the amount of metal ion adsorbed (mg/g) on each adsorbent. Eq. (5) provides the metal removal efficiency (E).

$$E = \frac{(C_o - C_e)}{C_o} \times 100 \tag{5}$$

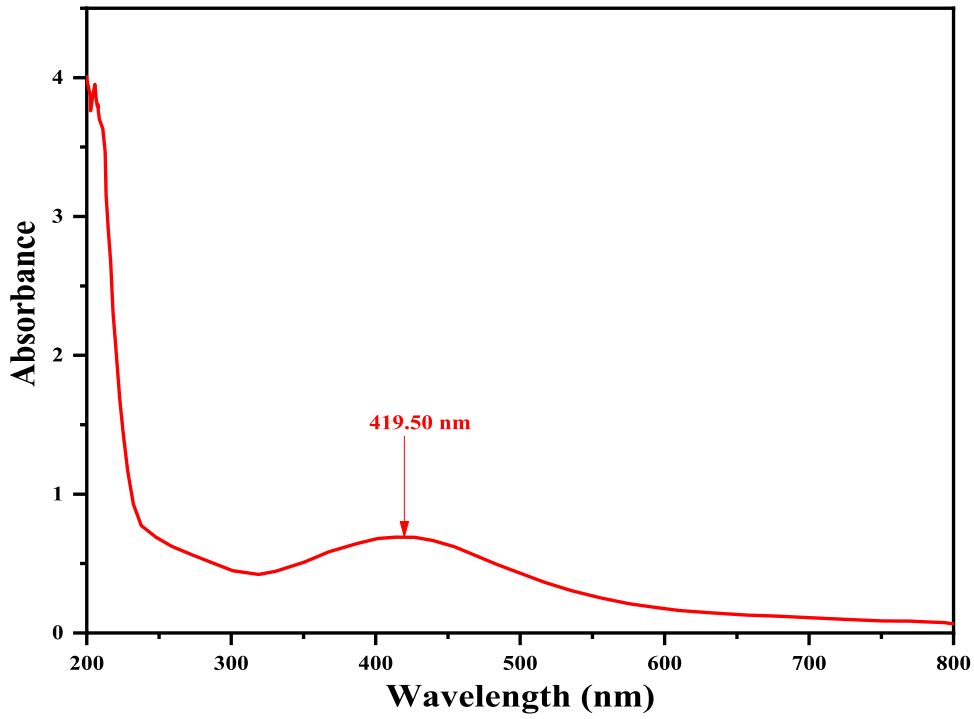

Fig. 1. UV–VIS spectrum of silver nanoparticles.

Table 1
The phytochemical constituents of pawpaw leaf extract.

Plant extract	Phytochemical	Concentration (mg/g)
Pawpaw leaf	Tannins	19.11 ± 0.13
	Flavonoid	3.73 ± 0.10
	Total Phenol	8.91 ± 0.21

where C_o and C_e are metal concentrations in the wastewater before and after adsorption in mg/L, respectively, and E is the percentage of metal removal.

3. Results and discussion

Phytochemical analysis of the extract

Table 1 presents the qualitative results of some phytochemicals, such as tannins, phenols, and flavonoids in the aqueous extract of pawpaw leaves. From Table 1, tannins had the maximum concentration levels (19.11 ± 0.13 mg/g), followed by phenols (8.91 ± 0.21 mg/g) and flavonoids (3.73 ± 0.10 mg/g), respectively. The phytochemical constituents of pawpaw leaf extract were also reported to be (0.001 ± 0.10 mg/g) for tannins, (0.011 ± 0.01 mg/g) for phenol, (0.013 ± 0.01 mg/g) for flavonoid by Bamisaye et al. (2013). According to several studies, these phytoconstituents play significant roles in the biochemical reduction of silver ions to silver nanoparticles as well as in stabilizing and capping the synthesized nanoparticles, which suggests that the phytochemical screening and quantitative estimation of the aqueous extracts of pawpaw leave obtained in this study were very rich in phenols, flavonoids, and tannins (Mohanta et al., 2017).

4. Synthesis of ag nanoparticles

UV-visible spectroscopy

A notable colour shift occurred during the biosynthesis of AgNPs. The $AgNO_3$ solution had no colour when it first started. The plant extract and the colour of the mixture turned brownish after 30 min of continuous stirring at 70 °C. This colour shift was regarded as proof that AgNPs had been successfully synthesized. Analysing the absorption spectrum of wavelength between 200 and 800 nm, as presented in Fig. 1, it was determined that silver nanoparticles were formed in an aqueous solution.

At 419.50 nm, there was a noticeable peak. The surface stimulation of the silver metal's plasmon resonance phenomena may cause the aqueous solution to change colour (Zargar et al., 2014). This happens due to the conduction electrons on the surface of the metal nanoparticles oscillating together when they align in resonance with the wave of irradiation light (Amendola et al., 2017). The characteristic colour of the nanoparticle is produced by the scattering and absorption of light at a certain frequency which is made possible by the combined oscillation of free electrons within the metal nanoparticles and the surface resonance.

X-ray diffraction

Fig. 2 depicts the XRD pattern of biosynthesized AgNPs from *Carica papaya* leaf extract. The XRD was used to determine the crystal structure of AgNPs, and the resulting diffraction peaks of various intensities were found at 2 theta angles of 38.35°, 44.87°, 64.83°, 77.76°, and 81.74°, representing (111), (200), (220), (311) and (222) face-centered cubic structures of silver. The results agreed with the literature (JCPDS card no-04-0783) and were similar to the XRD analysis of Chandhru et al. (2019). The bioreduction of silver nitrate and the synthesis of AgNPs are caused by interactions between these phytochemicals and silver ions.

From Fig. 2, the observed Bragg peaks might have resulted from some bioorganic compounds/proteins in the *Carica Papaya* leaf extract (Sagadevan et al., 2019). Using Debye Scherrer's equation in Eq. (6), the average Ag nanoparticle crystallite size was 11.35 ± 1.05 nm.

$$D = \frac{K\lambda}{\beta \cos\theta} \tag{6}$$

where D is the particle size, K is a dimensionless shape factor, its value is 0.94, λ is the X-ray wavelength (0.154 nm), β is full width half maximum (FWHM) of the peaks, and θ is the Bragg's angle.

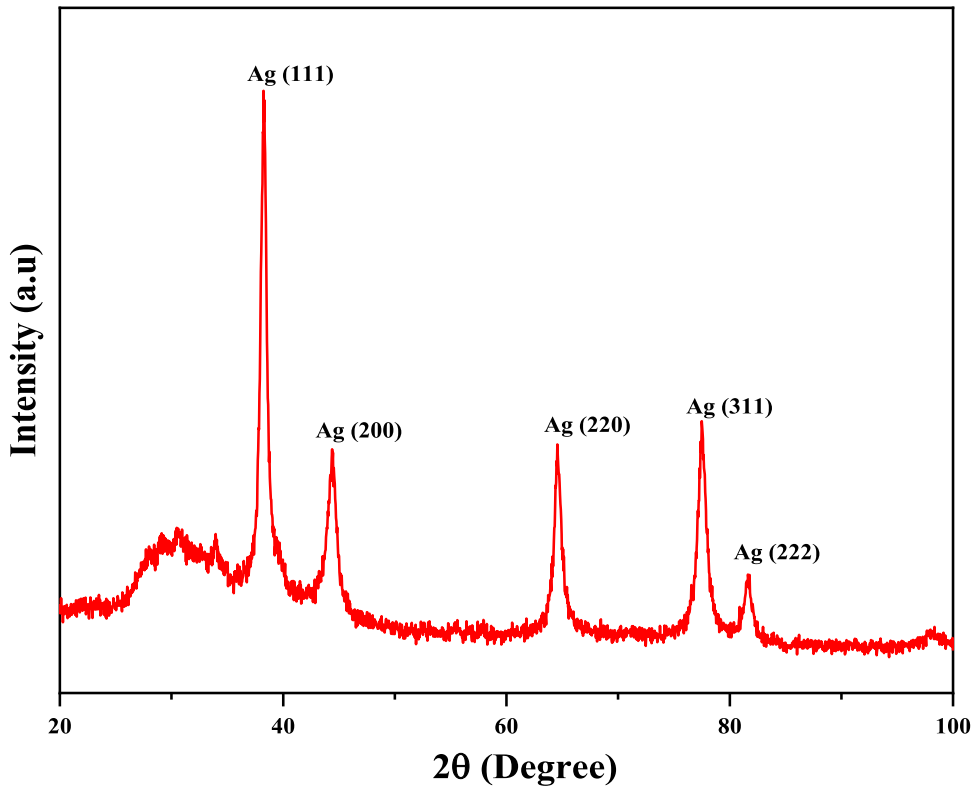

Fig. 2. XRD pattern of AgNPs.

HRTEM/EDX analysis

The HRTEM analysis was carried out to investigate the size and shape of biosynthesized silver nanoparticles presented in Fig. 3. The image showed clear and distinct spherical shapes of silver nanoparticles, with particle size distributions ranging from 11.12 to 15.39 nm for the magnifications represented in Fig. 3 (A_1 and B_2). Each of the diffraction rings in Fig. 3(c) was discovered to be consistent with the face-centered cubic structure of the Ag (111), (200), (220), (311), and (222) crystalline fringes. The particle size and SAED pattern of AgNPs agreed with the XRD results.

The EDX spectrum showed that the sample contained elemental silver (Fig. 4). The absorbance of silver nano-crystals is attributed to the surface Plasmon resonance, and the optical absorption of the silver metal peak in the EDX measurement was observed between ~3–4 Kev.

The surface hydroxyl group in the *Carica papaya* leaves may be the source of oxygen peaks in the EDX spectrum and the formation of carbon coupled with the carbon grid used during the EDX analysis. Other peaks (Ca and Si) that appeared were likely from the plant extract, and the grid used for the analysis must have caused the appearance of peaks for Cu and C.

XPS of silver nanoparticles

XPS was used to determine the surface oxidation state of each element contained in the produced silver nanoparticles, and the findings are displayed in Fig. 5.

XPS measurements were performed on AgNPs, and the sputtered sample of AgNPs shows the presence of C, O, and Ag, as shown in Fig. 5. As presented in Fig. 6(a), the C1s spectrum at 284.93 and 287.36 eV are attributed to the sp^2 bonded carbon (C–C) and carbonyl group (C=O), respectively. The spectrum of O1s (Fig. 6b) with peak at 532.31 eV indicates C=O. carbon was identified in the binding energy region of 284.93 eV, oxygen at 532.31 eV, and silver at 368.77 and 375.08 eV, respectively. Fig. 6(c) shows the spectrum of $Ag3d_{5/2}$ and $Ag3d_{3/2}$ for metallic related to 368.94 and 375.08 eV, respectively. Silver is a normal transitional metal with different electronic states; since its orbitals have large volumes, the energy required to give away electrons is significantly less. It is easy to give 2 electrons from the S orbital, forming a common oxidation state.

Table 2
XRF analysis of kaolin.

Oxide	Kaolin (wt %) (This study)	Kaolin (wt %) (Mamudu et al., 2020)	Kaolin (wt %) (Salahudeen, 2018)
SiO_2	54.21	58.50	52.04
Al_2O_3	28.43	16.62	27.81
Fe_2O_3	0.80	5.62	0.93
TiO_2	0.11	0.90	0.12
CaO	1.86	1.14	1.19
MgO	0.41	2.09	0.50
Na_2O	0.35	1.07	0.57
K_2O	3.90	1.50	1.89
MnO	0.03	0.01	-
BaO	0.73	-	–
SO_3	0.22	-	-
Cr_2O_3	0.04	-	-
V_2O_5	0.10	-	-
P_2O_5	-	0.10	-
CuO	-	0.02	0.02
LOI	8.81	12.35	14.70
Total	100.00	99.9	99.32

Production of CNTs

Characterization of kaolin

The support material (kaolin) was characterized to ascertain its appropriateness in CNTs production prior to the synthesis of bimetallic catalysts. Using the XRF technique, the oxide compositional analysis of the kaolin sample is displayed in Table 2. The elements in the kaolin sample and their respective percentages were noted, and the results show that silica (54.21%) and alumina (28.43%) are the two main components, respectively. Other oxides

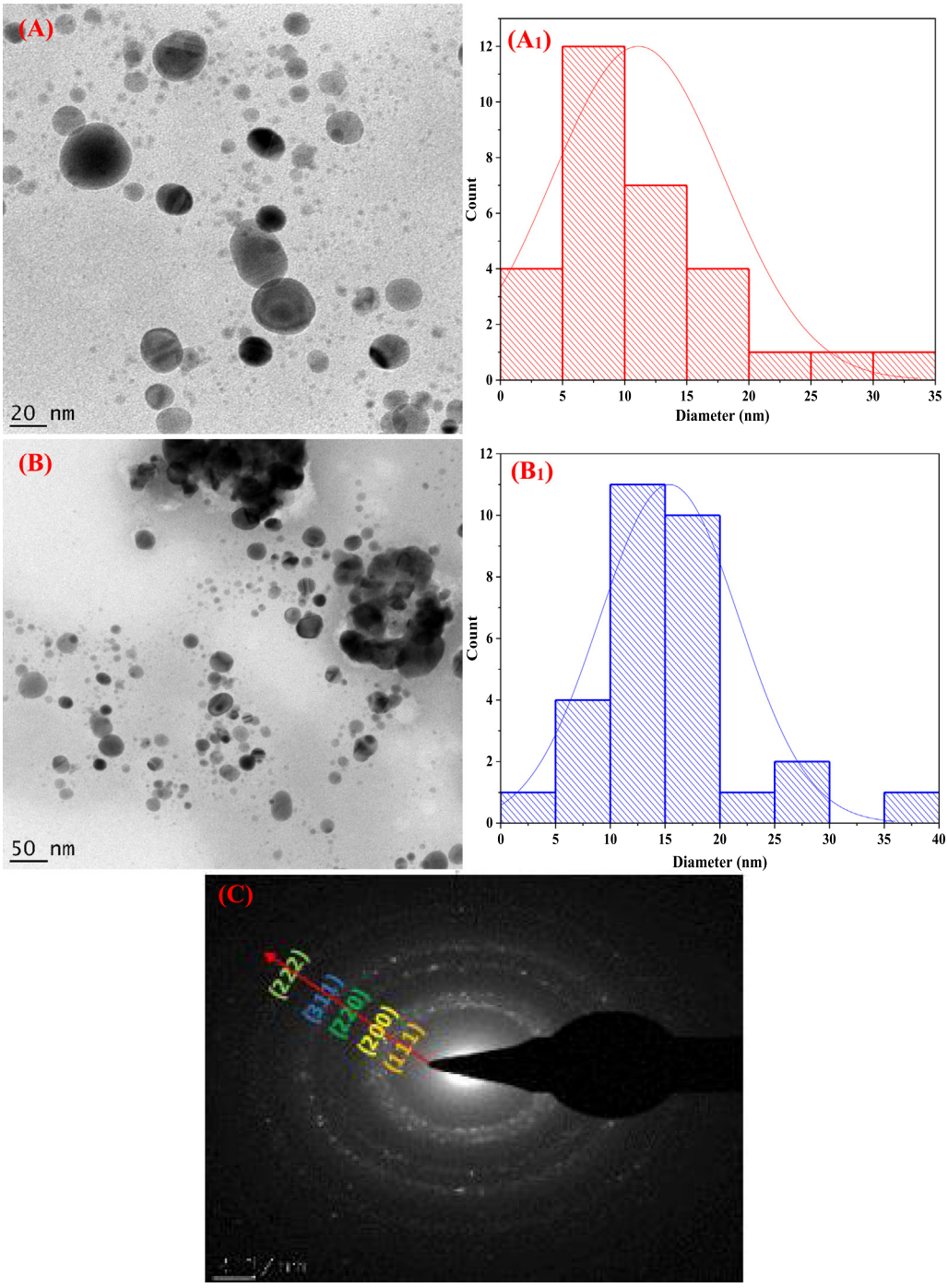

Fig. 3. TEM/SAED of synthesized AgNPS.

like iron oxide, potassium oxide, magnesium oxide, titanium oxide, calcium oxide, and barium oxide are in small quantities. The raw kaolin sample lost 8.81% of its volatile and organic content upon ignition, a loss on ignition (LOI) measurement. According to reports, kaolin has a more significant amount of silica, alumina, and titania and supports catalyst production due to its excellent thermal stability, large surface area, and porosity (Karim et al., 2018; Aliyu et al., 2017a). Thus, kaolin will enhance commercial support much more when used as catalyst support.

To comprehend the extent and suitability as a support material in the catalyst synthesis for the production of CNTs, it is crucial to determine the surface area, pore volume, and pore size distribution of the kaolin. According to Zhu et al. (2016a), more significant surface areas of supports lead to higher active metal dispersion, making them preferable. As shown in Table 3, the surface area of kaolin in this experiment was 11.56 m^2/g, and the pore volume and size corresponded to 0.00645 cm^3/g and 20.64, respectively. As a result, the kaolin offers a good surface area as catalyst support for the CCVD process of producing CNTs (see Table 4). .

The micrograph shows the aluminosilicate $[Al_2(Si_2O_7)(OH)_4]$, which is the main component in kaolin and has irregular particle morphologies and a plate-like character, as illustrated in Fig. 7.

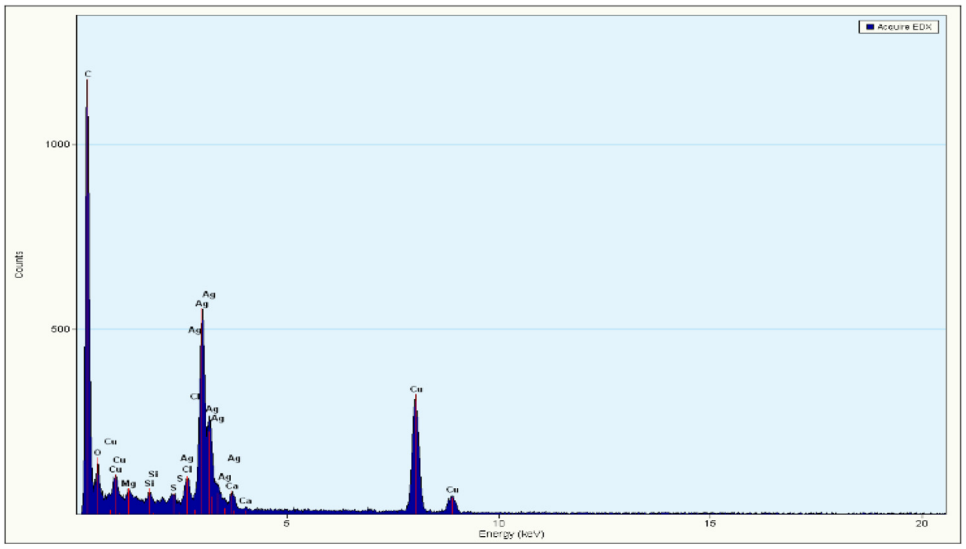

Fig. 4. EDX of AgNPs.

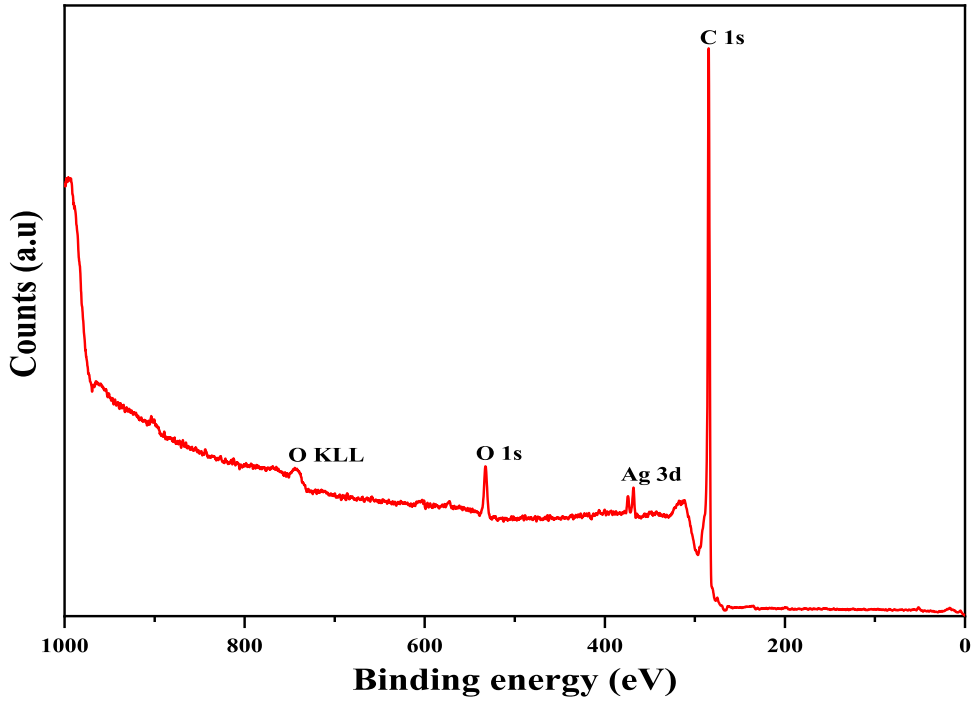

Fig. 5. XPS survey of AgNPs.

Table 3
BET value of kaolin.

Sample catalyst	Surface area (m^2/g)	Pore volume (cm^3)	Pore size (Å)
Kaolin	11.56	6.45×10^{-3}	20.64

The strong interaction connection in aluminosilicate material may be connected to the structure shown.

The crystal structure and phases of the kaolin sample were determined using XRD. In Fig. 8, the XRD pattern of the kaolin used in this study is presented, and it is observed from the XRD pattern that the kaolin was amorphous in nature. Numerous peaks at various diffraction angles and intensities are seen in the results in Fig. 8. As a result, quartz, muscovite, and kaolinite in the kaolin sample were identified. The kaolinite diffraction angles (2θ) are identified at 12.37, 20.43, 24.88, 36.16, 38.37, 54.88, and 60.43°. As presented in Table 2, the XRF results show the high capacity of silicon(IV) oxide, which conform to the identified phase (quartz) in the XRD result, will aid the synthesis of CNTs in this research study.

Characterization of Fe–Ni/kaolin catalyst

BET analysis of Fe-N/kaolin catalyst

FTIR of Fe–Ni/kaolin catalyst

Fig. 9 depicts the FTIR spectrum of Fe–Ni/kaolin catalyst. The band at 437 cm^{-1} was attributed to octahedral metal stretching, whereas the band at 591 cm^{-1} corresponds to intrinsic stretching

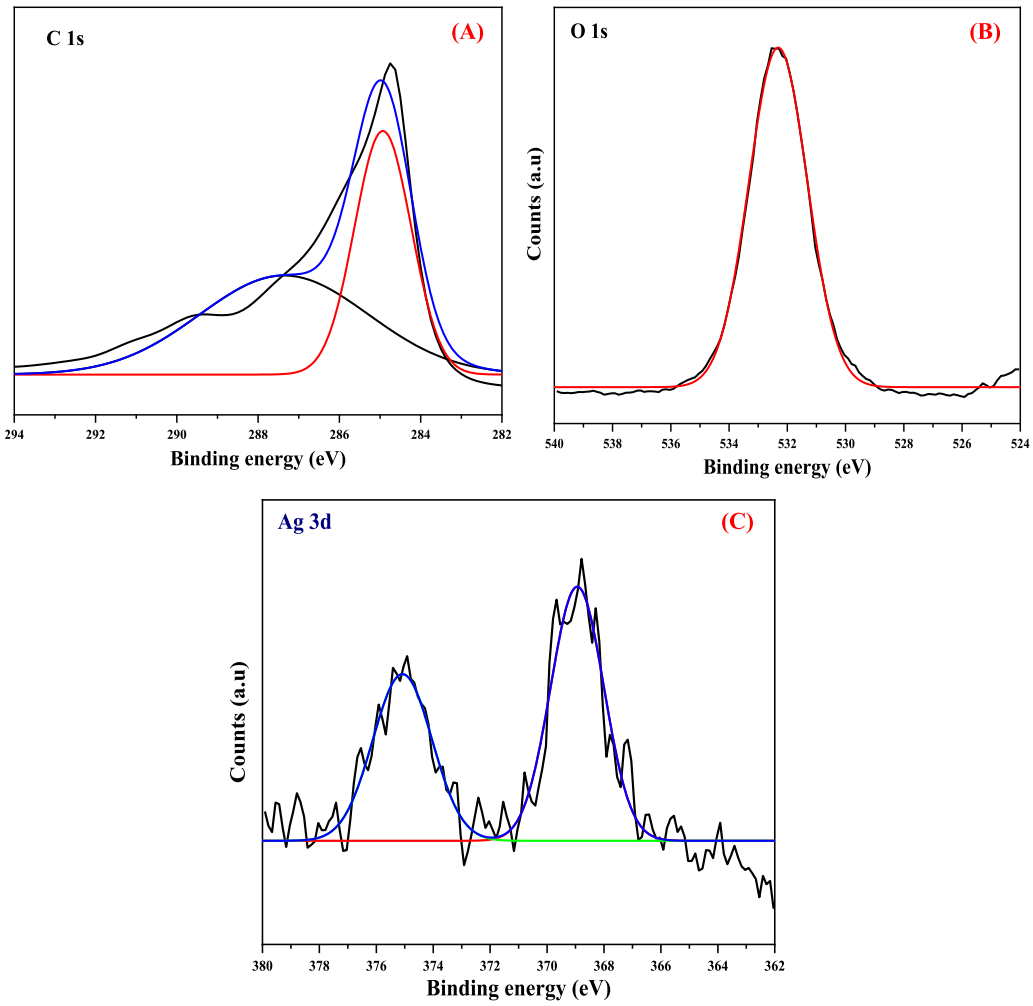

Fig. 6. XPS profile of AgNPs for (A) C 1s (B) O 1s and (C) Ag 3d.

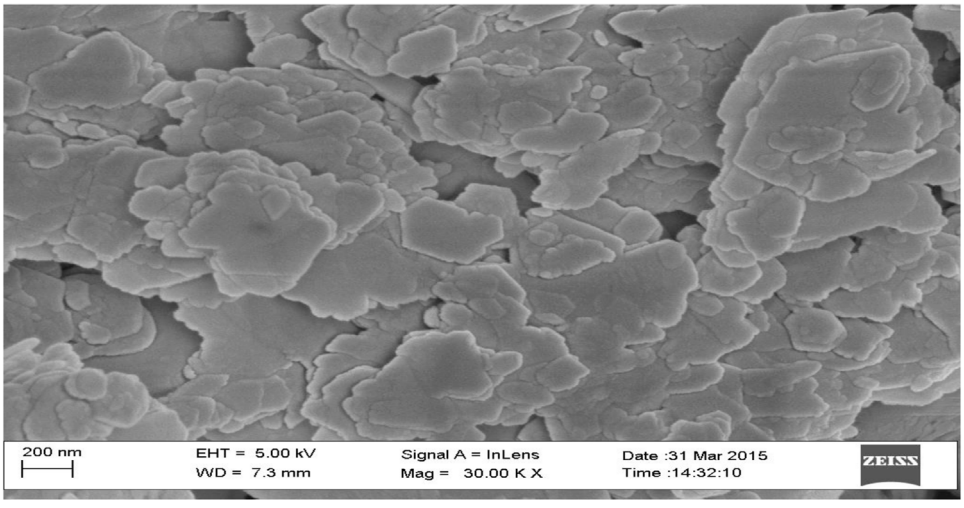

Fig. 7. HRSEM micrograph of kaolin sample.

Table 4
BET value of Fe–Ni/ Kaolin catalyst.

Sample catalyst	Surface area m^2/g	Pore volume cm3/g	Pore size (Å)
Fe–Ni/Kaolin catalyst	21.68	1.48×10^{-2}	25.99

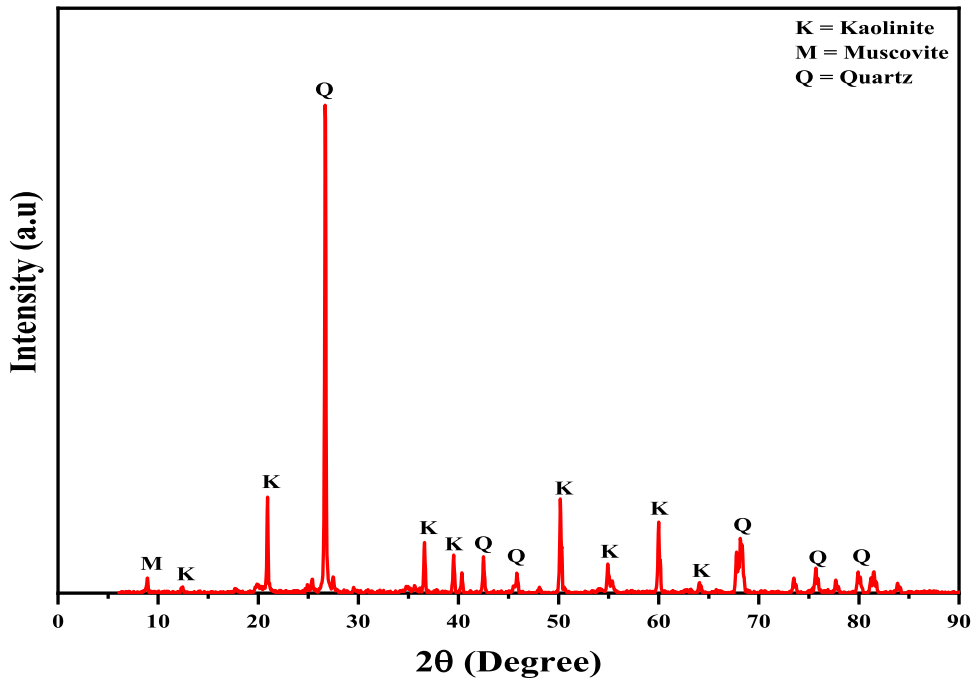

Fig. 8. XRD patterns of Kankara kaolin.

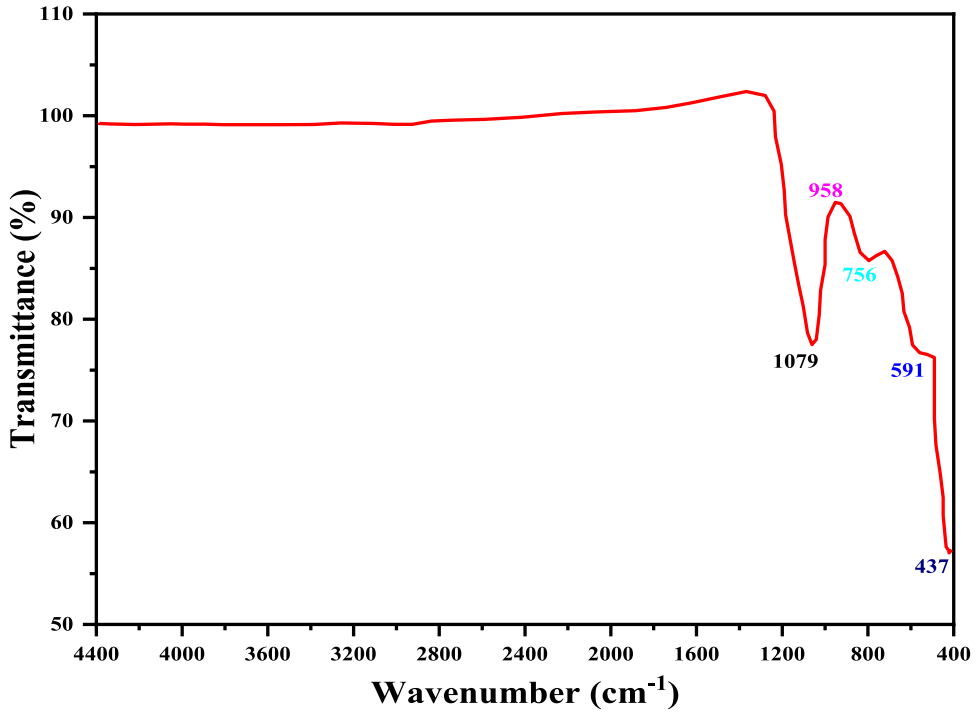

Fig. 9. FTIR spectrum of Fe–Ni/Kaolin catalyst by wet impregnation method.

vibrations of the metal at the tetrahedral site (Fe–O) and (Ni–O). According to Gunjakar et al. (2008), these two absorption bands are features of inverse spinel ferrites, and their positions in the infrared spectrum correlate to spinal $NiFe_2O_4$.

The presence of the Si-O-Si or Si-O-Al asymmetric stretching bands at 1079 cm^{-1} and 958 cm^{-1}, respectively, indicates the metal adsorption on the surface of the support material. The O-Al-O symmetric bending vibration is represented by the absorption band at 756 cm^{-1}.

HRSEM of the catalyst

Fig. 10 depicts the microscopic structure of the produced Fe–Ni/kaolin catalyst at different magnifications for a detailed micrograph of the catalyst sample. This figure shows that the nanoflakes metal catalyst was most evenly distributed on the surface of the kaolin support material, which is a crucial criterion for a catalyst to be used in the synthesis of CNTs.

EDX was used to perform elemental analysis on the prepared catalyst, as presented in Fig. 11. The results are consistent with the expected stoichiometry for the catalyst, demonstrating that all particles contained both Fe and Ni in a close wt.% ratio (50:50).

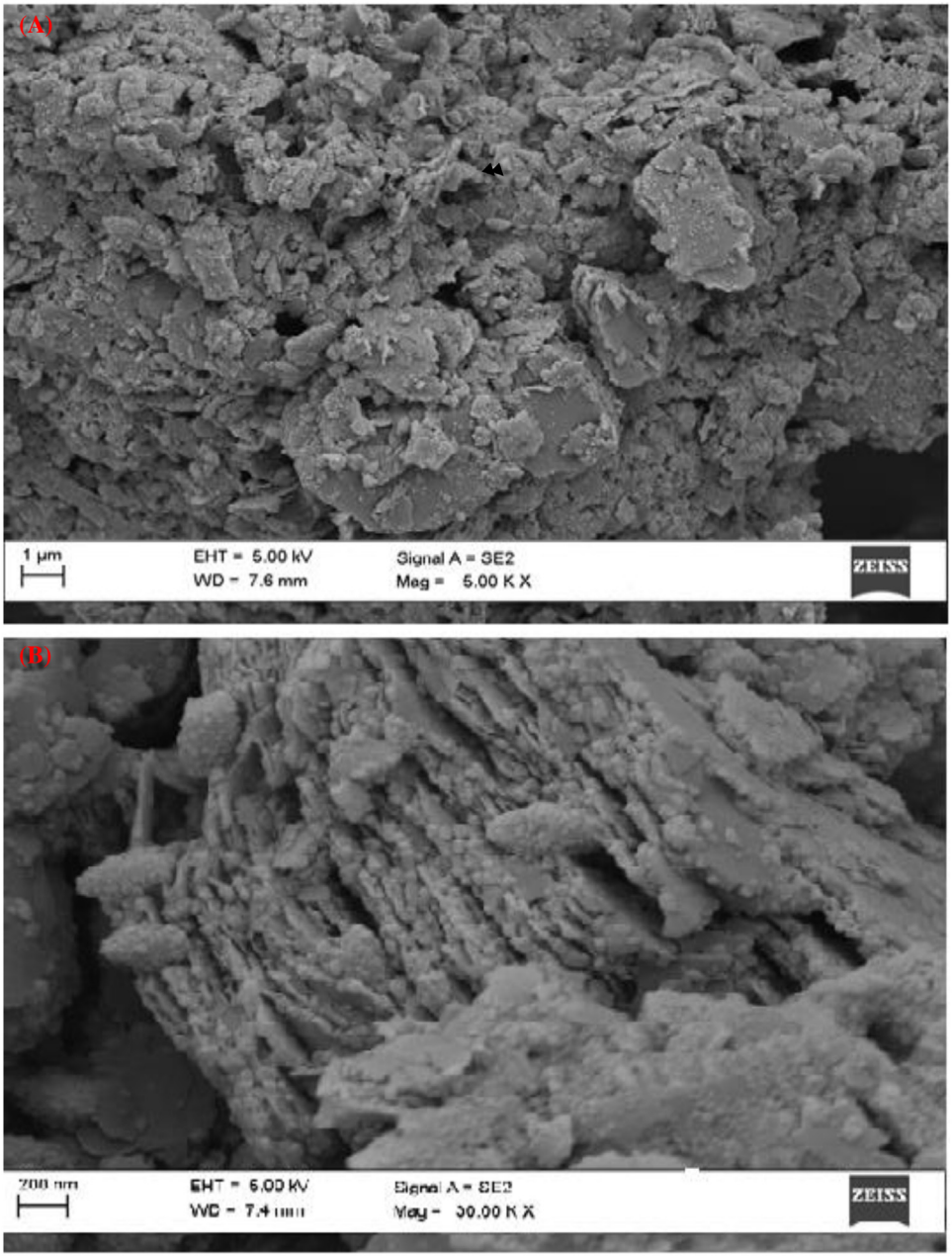

Fig. 10. The HRSEM image/micrograph of the Fe–Ni/kaolin catalyst.

The carbon grid served as a basis for the peaks that were assigned to carbon. According to Fig. 11, pure $NiFe_2O_4$was synthesized since the average atomic ratio of Ni to Fe was almost 1:1. The elements C, O, Mg, Ca, Fe, and Ni had the atomic percentage of 22.77, 61.38, 2.93, 7.38, 2.56, and 2.98, respectively may be present at lower energy levels, according to EDX. Oxides of the elements were present in the catalyst sample, contributing to the greater percentage weight of oxygen.

HRTEM/SAED analysis of the catalyst

In Fig. 12, it can be deduced that the pores and pore walls can be distinguished due to different densities; the dark region corresponds to the pore wall, and the bright one to the pore of the catalyst particles exhibited various sizes in the range of 29–33 nm. Also, the TEM images showed that some ($NiFe_2O_4$) particles had been effectively loaded on the kaolin.

The Fe–Ni/kaolin sample was calcined at 500 °C, and the SAED pattern of the sample is shown in Fig. 12. The lighter areas, which could be referred to as dense concentric ring regions, indicated the presence of iron and nickel particles. In comparison, darker areas could be identified as kaolin, as presented in Fig. 12. With each ring reflecting a distinct family of planes with a varied inter-planar separation, a series of concentric rings reflecting multiple spots very close together at various rotations around the center beam point was observed. The diffraction ring patterns observed in the SAED were indexed as (111), (211), (220), and (311) planes in the spinel structure (Fe–Ni). Thus, the diffraction pattern confirms the presence of Fe–Ni in the sample.

TGA analysis of synthesized CNTs

Fig. 13 (a–c) summarized TGA curves of as-synthesized CNTs, purified CNTs, and CNTs/AgNPs examined under an oxygen gas atmosphere.

From Fig. 13, the synthesized nanotubes consist of three regions; (a, b and c), the initial, main, and char decomposition regions. Water removal is the primary cause of the first weight

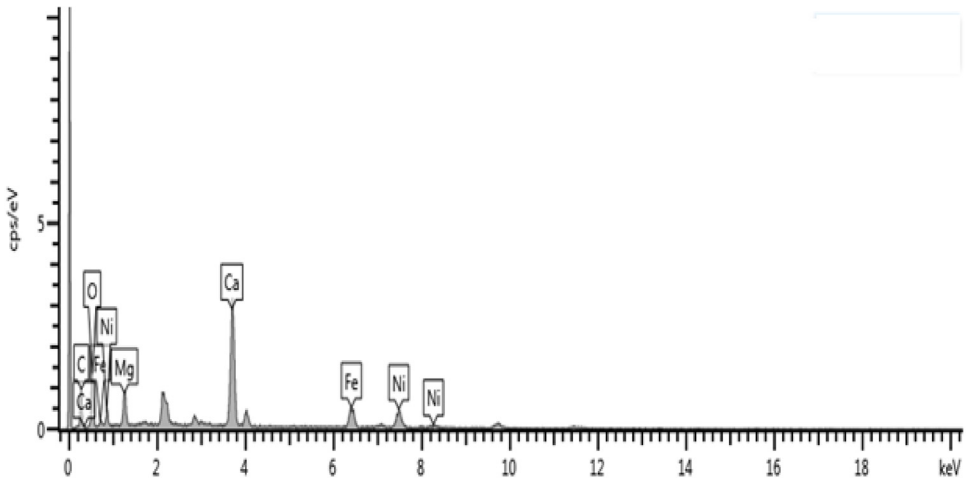

Fig. 11. An EDX spectrum of the Fe–Ni/kaolin catalyst.

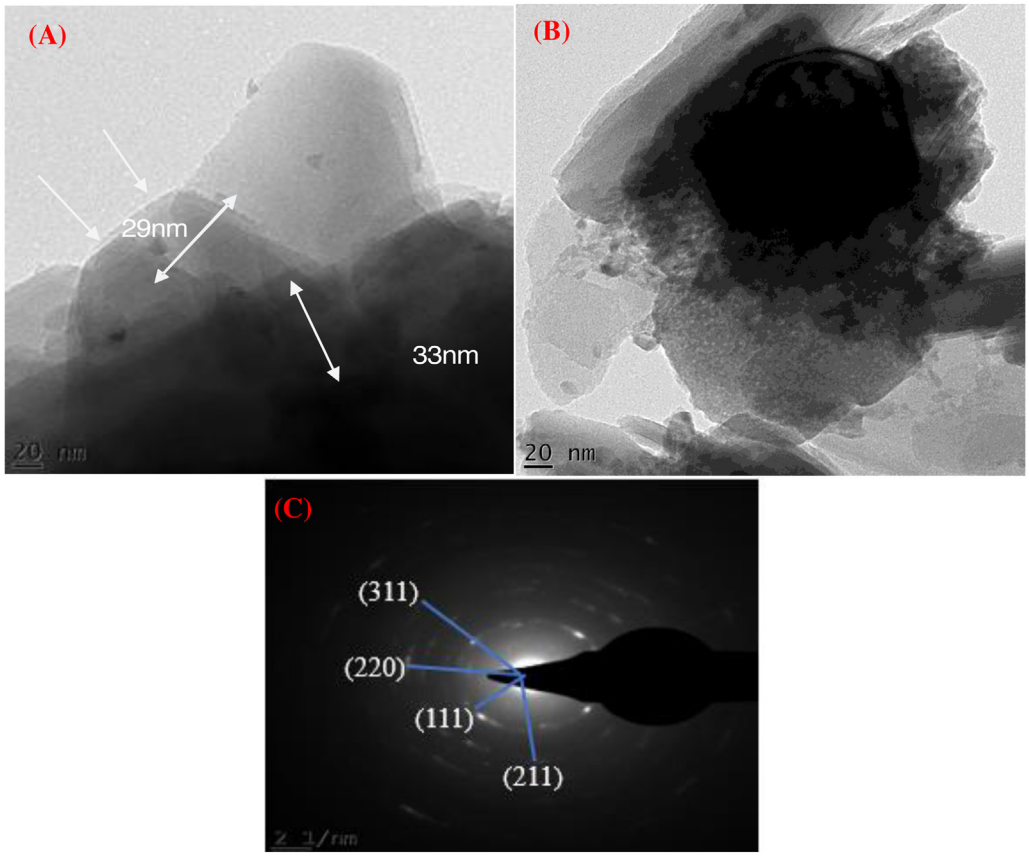

Fig. 12. RTEM and SAED of Fe–Ni/kaolin catalyst.

loss for both as-synthesized and purified CNTs at temperatures between 0 and 300 °C (ambient moisture). At temperatures between 300 and 420 °C, these altered thermal characteristics and weight loss of the sample result from some physical damage, primarily to the amorphous carbon component. Here, the second region is the primary thermal stage (when the weight loss is significant). However, Montazer et al. (2012) claimed that the TGA of as-produced CNTs varies on several factors, including uneven carbon cages, tube diameters, and structural defects.

Fig. 13(c) depicts the disintegration of Ag-doped CNT nanocomposites at a greater temperature than naturally occurring and pure carbon nanotubes. Although silver is an efficient oxidative catalyst because of its capacity to split oxygen molecules into atoms, it also provides sites for the oxidation of approaching chemical compounds by lightly adsorbing those atoms on the surface (Dey and Dhal, 2019). The residual mass of silver-doped CNTs examined was less than that of as-synthesized CNTs. The observed differences between as-synthesized and purified CNTs could be due to the thermal-oxidative destruction of the former, which resulted from the defect site along the CNTs wall. The purification process introduces the defect sites and provides the purified CNTs with enhanced air stability. Suggesting that after purification, the purity and crystalline carbon content of CNTs marginally rise from 63.83 to 69.76%. This further indicates that

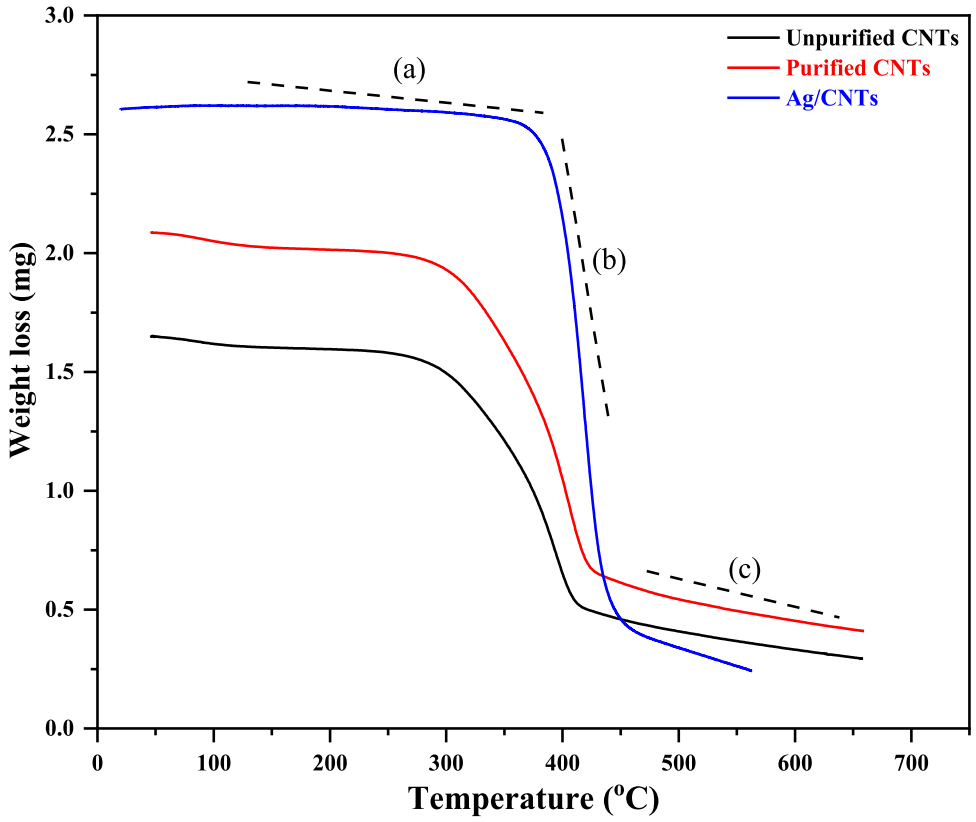

Fig. 13. TGA profiles of unpurified CNTs, purified CNTs, and Ag-CNTs.

Table 5
EDX analysis of carbon nanotubes.

Composite Samples	C	Ag	O	Al	Si	Ti	Fe	Ni	Cu
As-synthesized	91.59	–	3.02	1.41	1.35	0.05	1.62	0.86	0.10
P-CNTs	95.06	–	1.11	0.88	1.17	0.04	0.89	0.72	0.13
Ag-CNTs	85.82	5.65	5.86	0.9	0.87	0.08	0.45	0.26	0.11

pure CNTs are more thermally stable than CNTs that have been directly produced. In conclusion, the results of this investigation showed that the technique produced highly thermally stabilized Ag-CNTs that were not destroyed or derivatized by the deposition process (Verma and Maheshwari, 2019).

HRSEM/EDX analysis of synthesized CNTs

The HRSEM images, as presented in Fig. 14(a), show the possession of a long-strands curly branched tube-like structure of agglomerated carbon nanotubes, as indicated by arrows. An attempt was made to investigate the effectiveness of the purification process using the HRSEM techniques (Fig. 14b). The result demonstrates that P-CNTs are curved filaments braided into web-like structures with glossy tips. The image (Fig. 14c) also shows a typical structure with diameters ranging from 16 to 38 nm, one of the distinctive qualities of the MWCNTs produced using CVD procedures.

The HRSEM micrograph of Ag-CNTs, shown in Fig. 14(c), was taken to confirm the presence of produced nanoparticles on CNT surfaces. The image also shows that MWCNTs had reduced in size compared to purified CNTs after integrating silver nanoparticles, and they had maintained their tube-like form for a considerable time prior to its cleavage (Fig. 14c).

The atomic weight (%) of metallic silver deposited on the surface of the CNTs was 5.65% of the EDX result depicted in Table 5. The presence of C, O, Fe, and Ni, with a negligible quantity of metallic impurities, may be seen in the other elemental compositions of silver-doped CNTs.

HRTEM of synthesized CNTs

The HRTEM images of unpurified CNTs, purified CNTs, and silver-doped CNTs were obtained for detailed morphology and diameter of the materials. Fig. 15(a) reveals a representative HRTEM image of carbon deposits grown on the surface of kaolin-supported iron and nickel catalysts (as-synthesized CNTs). A high density of CNTs indicated a cluster of tube-like structures thickly covering the catalyst particles. The as-synthesized CNTs contain non-CNTs material, such as the residual growth catalyst and the catalyst support. The HRTEM results demonstrated that CNTs have variable wall structures and heterogeneous distribution of diameters. Additionally, Fig. 15(b) indicates that the purified CNTs consisted of numerous layers with a well-graphitized wall structure without any amorphous carbon covering.

The HRTEM analysis of Ag-doped CNT nanocomposites is shown in Fig. 15(c). It is noted that AgNPs were concentrated within the lattice fringes of the multilayer CNTs, further supported by the EDX result, as shown in Table 5. The distinctive morphological characteristics of these Ag nanoparticles are circular protrusions widely scattered on the grafted CNT surface.

Fig. 15 presents the SAED pattern of As-synthesized CNTs, purified CNTs, and Ag-doped CNTs. The SAED patterns of Ag-CNTs showed characteristic planes consistent with the planes reported in the XRD results and with the plane of (002), which indicates CNTs. The SAED patterns also reveal different concentric rings, which indicate the graphitic nature of the CNTs and the development of crystallinity of the Ag-CNTs nanocomposites. This

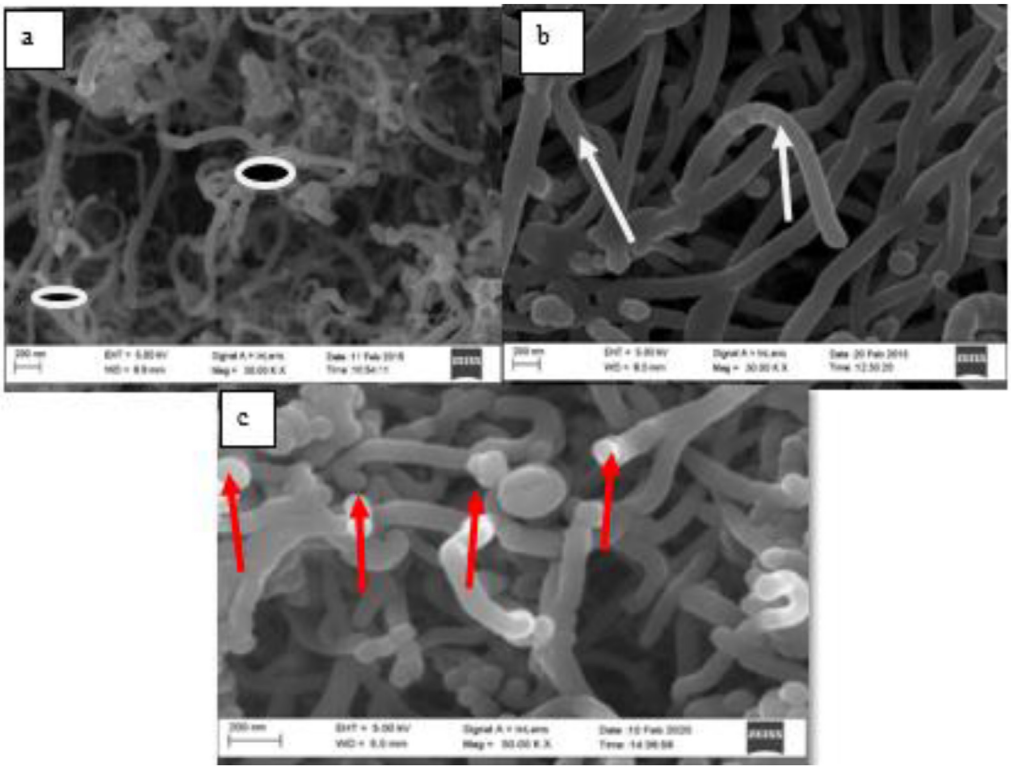

Fig. 14. HRSEM micrograph (a) unpurified CNT (b) purified CNTs(c) Ag-CNTs.

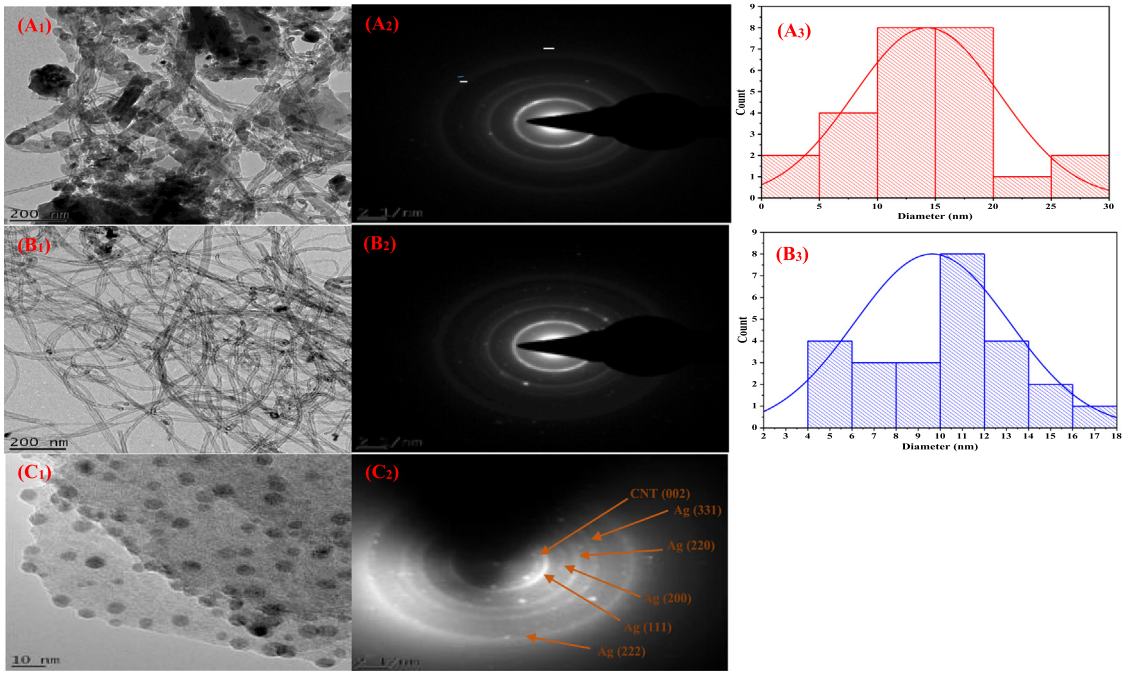

Fig. 15. HRTEM, SAED, and diameter distribution of (A) unpurified CNT (B) purified CNT (C) Ag-CNTs nanocomposites.

shows the polycrystallinity nature of the nanocomposite after encapsulating silver nanoparticles with CNTs. The HRTEM analysis of unpurified and purified CNTs is measured, and the particle size distribution shown in Fig. 15 is 12.45 and 10.98 nm, respectively.

XRD analysis of synthesized CNTs

Powdered XRD techniques were used to further analyse the as-synthesized unpurified CNTs, purified CNTs, and Ag-doped CNTs to confirm their mineralogical phases. Only two distinct diffraction angles could be seen in the XRD patterns of the samples of as-produced CNTs, as shown in Fig. 16. The patterns show major peaks around the 2θ value of 26° and 44° with a corresponding plane of (002) and (100), which are usually characteristic planes for graphite-like carbon of the CNTs. The peaks found at 30.49°, 52.68°, and 61.80° are indexed as the (110), (220), and (211)

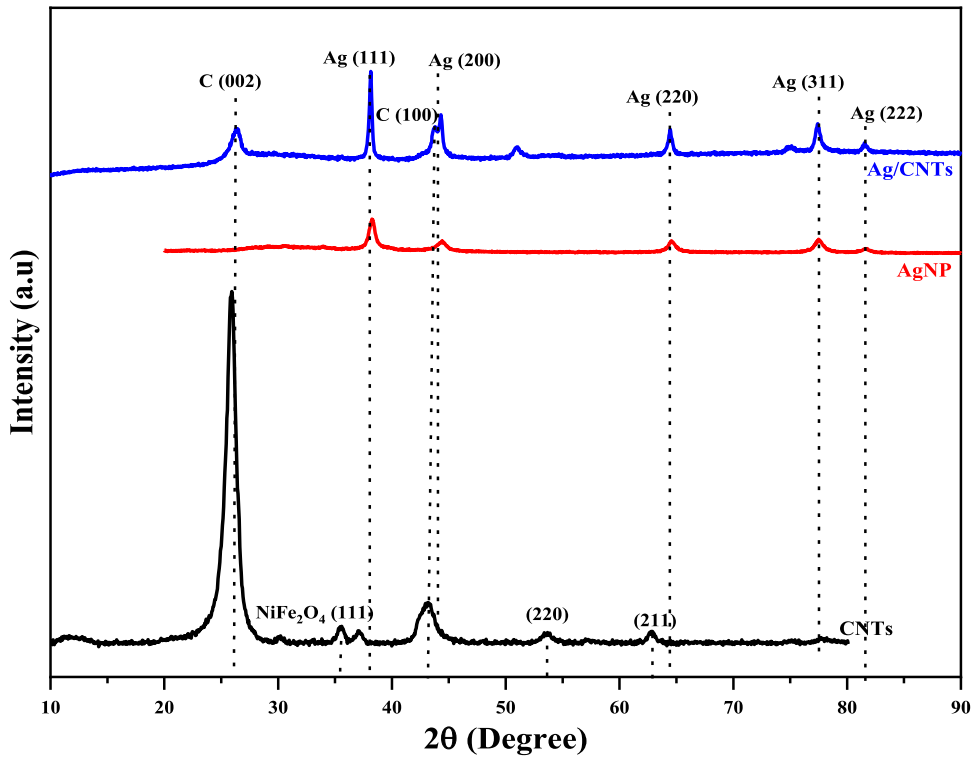

Fig. 16. XRD patterns of (a) as-synthesized CNTs (b) P-CNTs (c) Ag-CNTs.

planes of kaolin. The peak around 34.88°can be assigned to the (111) reflection of bi-metallic oxide ($NiFe_2O_4$)

Also, in Fig. 16 for the purified CNTs, the peaks appeared at 26.2°, 43.47°, and 74.72° are indexed as the (002), (100), and (204) planes of carbon, respectively; it was observed that more peaks of carbon came up which might be as a result of the removal of residue metal particles from the as-synthesized CNTs. Fig. 16 displays similar XRD findings for the Ag-CNTs. At a 2-theta value of 26.30°, a distinctive peak was attributed to the (002) plane of CNTs. The Ag reflection planes of (111), (200), (220), (311), and (222) are attributed to the peaks at 38.35°, 44.87°, 64.83°, 77.76°, and 81.74°, respectively. The additional peaks around the reflection angles of Ag-CNTs suggest that the produced adsorbent could transpire to the crystal lattice of the material. This observed phenomenon in the Ag-CNT composite XRD patterns corresponds to the SAED pattern in Fig. 15. However, the crystallite sizes of the unpurified and purified CNTs were calculated from the XRD patterns based on the Debye Scherrer equation, and the results showed the average crystallite sizes of 13.14 nm and 11.80 nm, respectively.

FTIR of as-synthesized and purified CNTs

Chemical substance surface functional group identification was analysed using the FTIR spectrum in Fig. 17. In the Ag-CNTs, the –OH vibrational bond is indicated at the band wavenumber at 3894 cm^{-1}, and C-H stretching is consistent with the wavenumber of 2848 cm^{-1}. The band wave number at 3759 cm^{-1} suggests the –OH vibrational bond for the CNTs is slightly higher than 3688 cm^{-1} as identified for Ag-CNTs. A peak around 1395 cm^{-1} corresponds to the C–C stretching, showing interaction and surface disruption brought on by the adhesion of metal particles, and the Ag–O peak appears at 870 cm^{-1}. The Ag-CNTs spectrum shows that silver deposition on MWCNTs increased the strength of the bands and pushed them towards lower wave numbers. This modification results from a charge-transfer process and chemical contact between the surfaces of the MWCNTs and the AgNPs after the deposition operation. The C–C bending was also observed at 1589.98 cm^{-1} for unpurified and purified CNTs. In comparison, the presence of C–C (1395 cm^{-1}) and C=C (1926 cm^{-1}) was connected to the synthesized Ag-CNTs could be due to incomplete acetylene decomposition during catalytic cracking of the gaseous hydrocarbon material.

Table 6
BET analysis.

	As-synthesized CNTs	P- CNTs	Ag-CNTs
BET surface area (m^2/g)	244.40	268.40	1068
Pore volume (cm^3/g)	0.086	0.105	0.381
Pore size (nm)	3.040	3.287	6.503

BET analysis of synthesized CNTs

The surface area, pore volume, and pore size of the prepared materials (as-synthesized are presented in Table 6.

The N_2 adsorption–desorption isotherms of the CNTs as-synthesized, the purified CNTs, and the Ag-CNTs are type IV hysteresis loops, demonstrating the mesoporous features of the nanomaterials. The as-produced CNTs had a 244.4 m^2/g BET surface area. The BET surface area was measured to be 268.40 m^2/g following purification. The findings show that the purifying procedure enhanced the surface area of the nanoadsorbents (Burakova et al., 2018). The more active sites on the adsorbent surfaces could result from the higher specific surface area, which would be advantageous for the occurrence of the redox reaction and enhance its capacitance performance (Cuong et al., 2020). Additionally, the larger pores of purified CNTs make it easier for particles to move about during the adsorption process, improving the efficacy of the adsorbent (Li et al., 2016). Silver-doped CNTs had a BET surface area of 1068 m^2/g, indicating a greater surface area increase. Silver nanoparticles doped on the surface of CNTs may be responsible for this increase in the surface area because they have hollow shapes and a lower density than synthesized nanoparticles. According to the International Union of Pure and Applied Chemistry (IUPAC), materials with pores

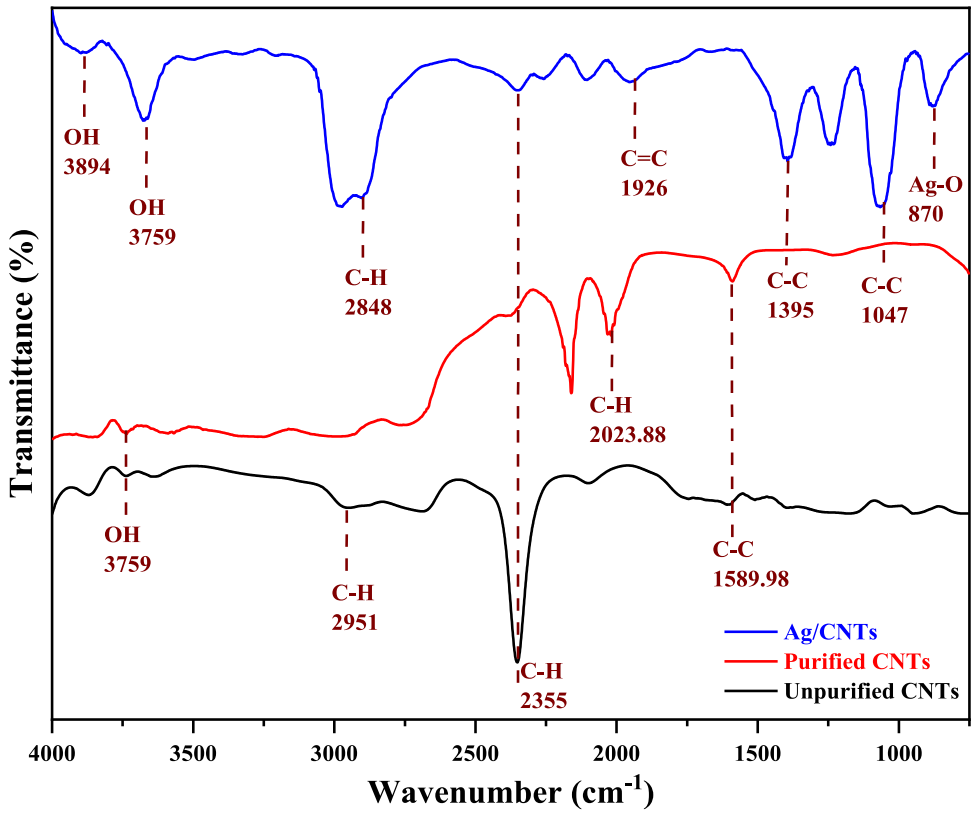

Fig. 17. FTIR spectra of unpurified CNTs, purified CNT and Ag-CNT.

less than 2 nm are classified as microporous, those between 2 and 50 nm as mesoporous, and those larger than 50 nm as mesoporous macroporous. As a result, the synthesized nanoadsorbents in this study revealed that they are mesoporous in nature (Table 6). In general, the obtained result of the pure CNTs confirmed the effectiveness of the purification process. A similar observation was reported by Aliyu et al. (2017b), who reported an increase in the surface area of CNTs after purification.

Physicochemical parameters of fish pond wastewater before and after adsorptions

The wastewater samples were characterized for their physicochemical properties before and after the adsorption process results, as presented in Table 7, along with the maximum required limit for drinking water reported by World Health Organization (WHO) and Anon (2009).

The pH of the fish pond wastewater sample was 7.88. While the pH value varied between 6.74 and 6.61 in the treated wastewater samples using P-CNTs and Ag-CNTs, respectively. After treatment, the pH values fall within the acceptable ranges established by NESREA guidelines (6.5–8.5), demonstrating that the treated wastewater sample is nearly neutral. The solubility and biological availability of chemical compounds like nutrients and heavy metals are directly influenced by pH measurement. The toxicity of heavy metals is based on how soluble they are. The highly acidic or alkaline substance would impact the solubility, mobility, and metal toxicity of water and consequently destroy marine life in the ecosystem (Lokhande et al., 2011). As a result, pH measurement has specific crucial characteristics that help determine wastewater quality. According to WHO guidelines, most aquatic organisms can survive in water with a pH of 6.5 to 8.5, whereas the pH range for treated water is tolerable for humans. This fact leads to the conclusion that the treated water can be used again for various domestic activities.

The inorganic and organic particles in water make up the total soluble solids. The raw wastewater sample for this sample had a total dissolved solids (TDS) value of 240 mg/L as opposed to the WHO and NESREA standard of 500 mg/L. The TDS values of the treated wastewater for P-CNTs and Ag-CNTs were 3.00 mg/L and 2.83 mg/L, respectively, after the wastewater sample was treated using nanoadsorbents. According to the results, the TDS concentration readings are below the NESREA-permissible limit of 500 mg/L. TDS provides a quantity of dissolved organic and inorganic substances, which can raise the turbidity of water (Khan et al. 2013). In water bodies, salts are dissolved and are known to make the water denser and influence freshwater osmoregulation in aquatic organisms, decreasing the supply and usefulness of oxygen and water for drinking, irrigation, and other industrial uses. When dissolved minerals like calcium, chloride, and magnesium are present in water samples, the water conductivity increase, thus influencing the ability of any medium to transport an electric current. The maximum permissible conductivity level is 200 μS/cm, according to WHO and NESREA. According to this study, treated water samples have a measured conductivity of 6.82 μS/cm for P-CNTs and 7.94 μS/cm for Ag-CNTs, compared to 397 μS/cm for effluent sample. Although conductivity has no direct impact on human health, high conductivity may reduce the aesthetic value of water by imparting a mineral taste to it (Rahmanian et al., 2015).

Aquaculture effluent had much greater levels of dissolved oxygen, biological oxygen demand, and chemical oxygen demand than values seen in wastewater treatment. The capacity of nanoadsorbents to remove nutrients and other contaminants from aquaculture wastewater may cause these variations. This suggests that the toxins in wastewater from aquaculture are biodegradable. The low level of DO measurement is 3.07 mg/L, which could be due to high levels of chemical oxidation demand and aerobic microbial activity (BOD), two pollution indicators.

Table 7
Physicochemical parameters of fish pond wastewater before and after treatment with the maximum permissible limit at different conditions of dosage (0.4 g/50 cm^3) Temperature at 60 °C, contact time of 100 min, and stirring speed of (120 rpm).

Parameters	Raw water	Treatment using P-CNT	Treatment using Ag-CNT	World Health Organization (WHO)/ Anon (2009)
pH	7.88	6.74	6.61	6.5–8.5
Conductivity (μs/cm)	397	7.94	6.82	200
Nitrate (mg/L)	6.22	0.56	0.51	10
Phosphate (mg/L)	1.66	0.02	0.01	0.5
Chloride (mg/L)	252.57	8.31	9.70	250
DO (mg/L)	3.07	6.48	8.0	8-10
BOD (mg/L)	6.50	4.50	3.8	10/5–7
COD (mg/L)	42.64	39.25	35.75	40
TDS (mg/L)	240.10	3.00	2.83	500
Manganese (mg/L)	1.435	0.73	0.144	0.40
Zinc (mg/L)	3.75	2.56	1.22	3.00
Iron (mg/L)	4.43	0.64	0.108	0.3
Bacteria (cfu/ml)	7.2×10^2	65.0	0.00	–
TA (mg/L)	78	15.23	5.53	0–0.05
Ca (mg/L)	54.68	56.90	49.62	25–200
Na (mg/L)	16.59	13.96	13.72	200
K (mg/L)	3.80	3.24	3.19	12
Mg (mg/L)	10.41	10.36	8.48	50

Omitoyin et al. (2017) showed lower DO in wastewater drained from shrimp ponds, ranging from 3.00 mg/L to 3.20 mg/L. This is due to increasing levels of biodegradable organic materials in the wastewater discharged from unconsumed feed, fish feces, and metabolites from microbial activities. The high COD in aquaculture wastewater may be attributed to increased organic matter. However, the low BOD value of wastewater was recorded as 6.50 mg/L, which is higher than the value obtained from the treated wastewater of 0.75 mg/L and 0.5 mg/L for P-CNTs and Ag-CNTs, respectively. Although the COD in wastewater value (42.64 mg/L) was greater than the WHO and NESREA standard (40 mg/L) and values of treated wastewater, which are 0.03 mg/L and 0.01 mg/L for P-CNTs and Ag-CNTs, respectively,

The fact that indicators like phosphate, nitrate, and total alkalinity (TA) were higher in the wastewater than in the treated wastewater suggests that fish meal, which is a protein-rich feed constituent, may have leached nutrients. The wastewater has a phosphate value of 1.66 mg/L, greater than the phosphate values of 0.02 mg/L and 0.01 mg/L for P-CNTs and Ag-CNTs, respectively, for the treated wastewater. According to the literature, more than 1 mg/L phosphate concentrations could stop sewage from coagulating in a water treatment system (Omitoyin et al., 2017). The nitrate level of 6.22 mg/L found in wastewater was higher than the values of 0.56 mg/L and 0.51 mg/L for P-CNTs and Ag-CNTs, respectively, found in treated wastewater. The TA values for the treated water, which were significantly lower than the value for the wastewater in this investigation, are 15.23 mg/L for P-CNTs and 5.53 mg/L for Ag-CNTs, respectively. The results of the bacterial analysis suggested that the bacterial count may be related to variations in management strategies that result in varying levels of organic loads in the pond system from the fish diet (Oni et al., 2013). The source of bacteria might be traced back to water sources flowing into the pond. Bacterial counts of aquaculture wastewater were 7.2×10^2 cfu/mL, much higher than the values of treated wastewater, which are 65.0 cfu/mL and 0.00 cfu/mL for P-CNTs and Ag-CNTs, respectively. However, in this study, the chloride ion is 252.57 mg/Lin in the wastewater, which is slightly beyond the acceptable limit of Anon (2009) guideline value (250 mg/L), and the chloride value in treated water is 8.31 mg/L and 9.70 mg/L for P-CNTs and Ag-CNTs respectively.

To address this issue, it is necessary to completely remove or significantly reduce the level of these contaminants in the wastewater before final discharge into the environment. Table 7 shows the concentration of the selected heavy metal in aquaculture wastewater and reveals these metals in different proportions. For the adsorption of the selected heavy metals, synthesized nanomaterials were used as the adsorbent.

Adsorption studies

This study investigated the influence of parameters such as contact time, adsorbent dosage, and temperature on the removal efficiency of the selected heavy metals by nano-adsorbents.

Effect of contact time

The effect of contact time (0 to 120 min) on nano-adsorbents is shown in Fig. 18(a) and (b). It can be seen from Fig. 18(a) and (b) that heavy metal removal increases slightly with time, irrespective of the nano-adsorbents. In the figures, a very fast adsorption rate was noticed, and the optimum time for removal of Mn, Zn, and Fe is 100 min for both P-CNTs and Ag-CNTs.

The optimal time for removing the three metals (Mn, Zn, and Fe) for the P-CNTs is 100 min. At this stage, the heavy metals adsorbed onto the CNTs counterbalanced the heavy metals desorbing from the adsorbent. The heavy metals adsorbed at the equilibrium time represents the maximum adsorption capacity of the adsorbent under operating conditions. The time necessary to reach this state of equilibrium is referred to as the equilibrium time.

Fig. 18(a) illustrates the effectiveness of pollutant removal in relation to treatment time. Zn (91.20%), Fe (82.10%), and Mn (50.25%) had the highest percentage reductions after a total of 100 min of treatment. The initial concentration of heavy metals in the wastewater, which is essential to the mass transfer of molecules from the liquid to the solid surface during the adsorption process and is also time-dependent, may cause the higher value of Mn. At 100 min, Mn, Zn, and Fe reached this equilibrium. The porous nature of the nanoadsorbent contributes to its capacity for adsorption, along with various interfaces that depend on the porous nature of the adsorbent and the features of the adsorbate, such as hydrogen bonding, cation exchange, electrostatic attraction, surface precipitation, and among others. The adsorbent sites displayed an affinity towards saturation and equilibrium as the treatment period rose, which described the adsorbent–adsorbate affinity (Anijiofor et al., 2018). In other words, a high driving force that results in a quick transfer mechanism between the adsorbed metals and the active site of the adsorbent may be the cause of a fast initial adsorption rate.

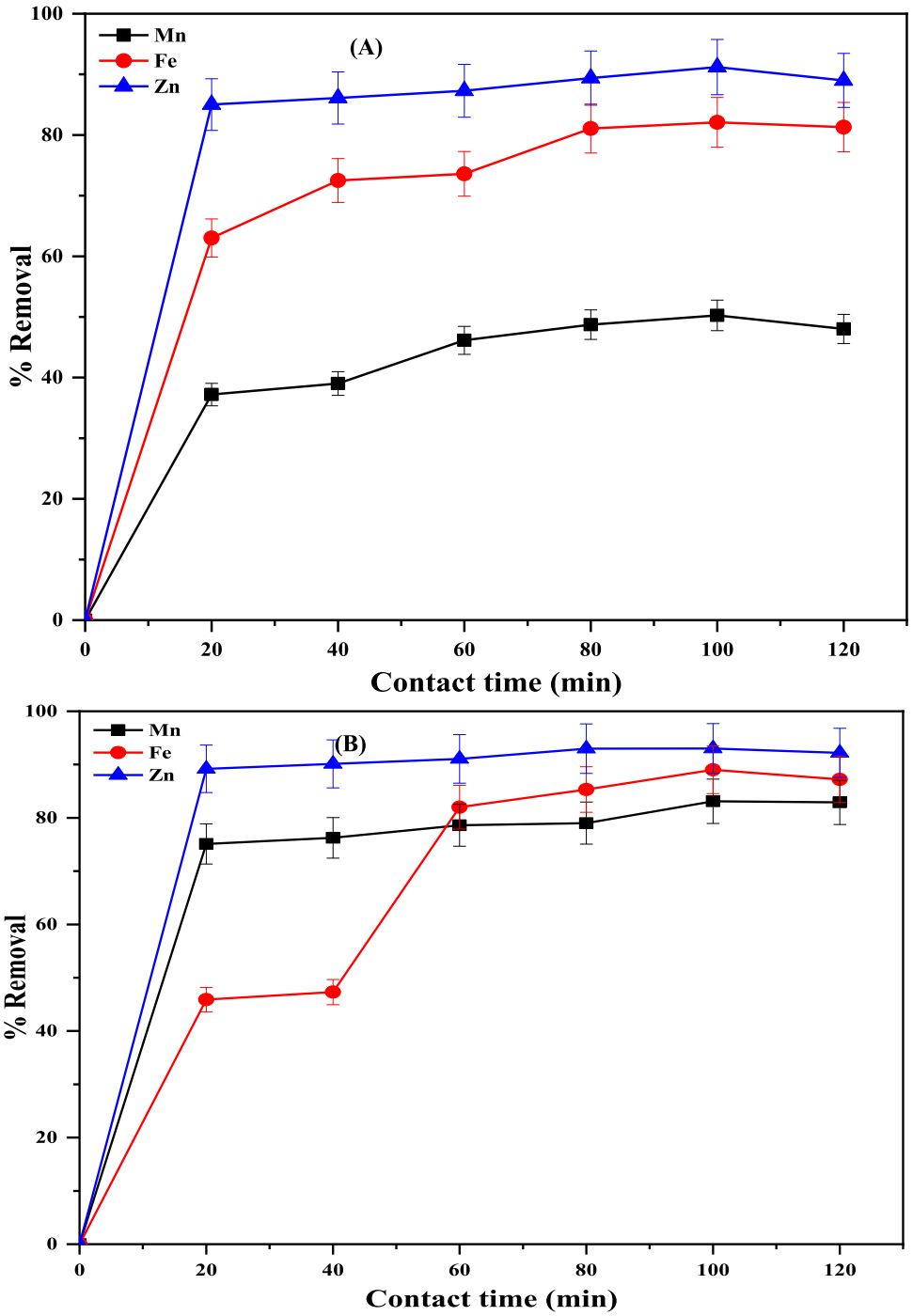

Fig. 18. Effect of contact time of heavy metals using (a) P-CNT (b) Ag-CNT (adsorbent dosage (0.1 g), stirrer speed (120 rpm), and temperature (25 °C) volume of fish pond wastewater (50 cm^3), stirring time (90 min).

Fig. 18(b) also shows that as the contact time increases, a corresponding increase in the adsorption of the selected heavy metals was observed. It can also be observed at the initial stages, the slope was greater and later decreased with time, suggesting that the rate of adsorption was rapid in the initial stages and subsequently attained the optimum at 100 min, amounting to Zn (93.02%), Mn (83.10%) and Fe (89.01%), respectively. The order of adsorption of heavy metals using Ag-CNTs in decreasing order is Zn (1.53 Å) > Fe (1.72 Å) > Mn (1.79 Å), which could be attributed to a decreasing ionic radius of the heavy metals. It can be seen that equilibrium time is metal-dependent adsorbent specific. The adsorption of heavy metals on Ag-CNTs was therefore thought to be complete after 100 min. More metal ions were successfully removed by Ag-CNTs than P-CNTs, indicating a higher interaction between the adsorbent and adsorbate in the former. Alternately, the considerable surface area and pore diameters of Ag-CNTs (BET results in Table 6), the high crystallinity of TEM and XRD, and the presence of the functional groups may all contribute to their high adsorption rate.

Effect of adsorbent dosage

The adsorbent dosage parameter has a pronounced effect on removing adsorbate species from wastewater. This study investigated the effects of different P-CNTs dosages (from 0.1–0.5 g) on the selected heavy metals removal from fish pond

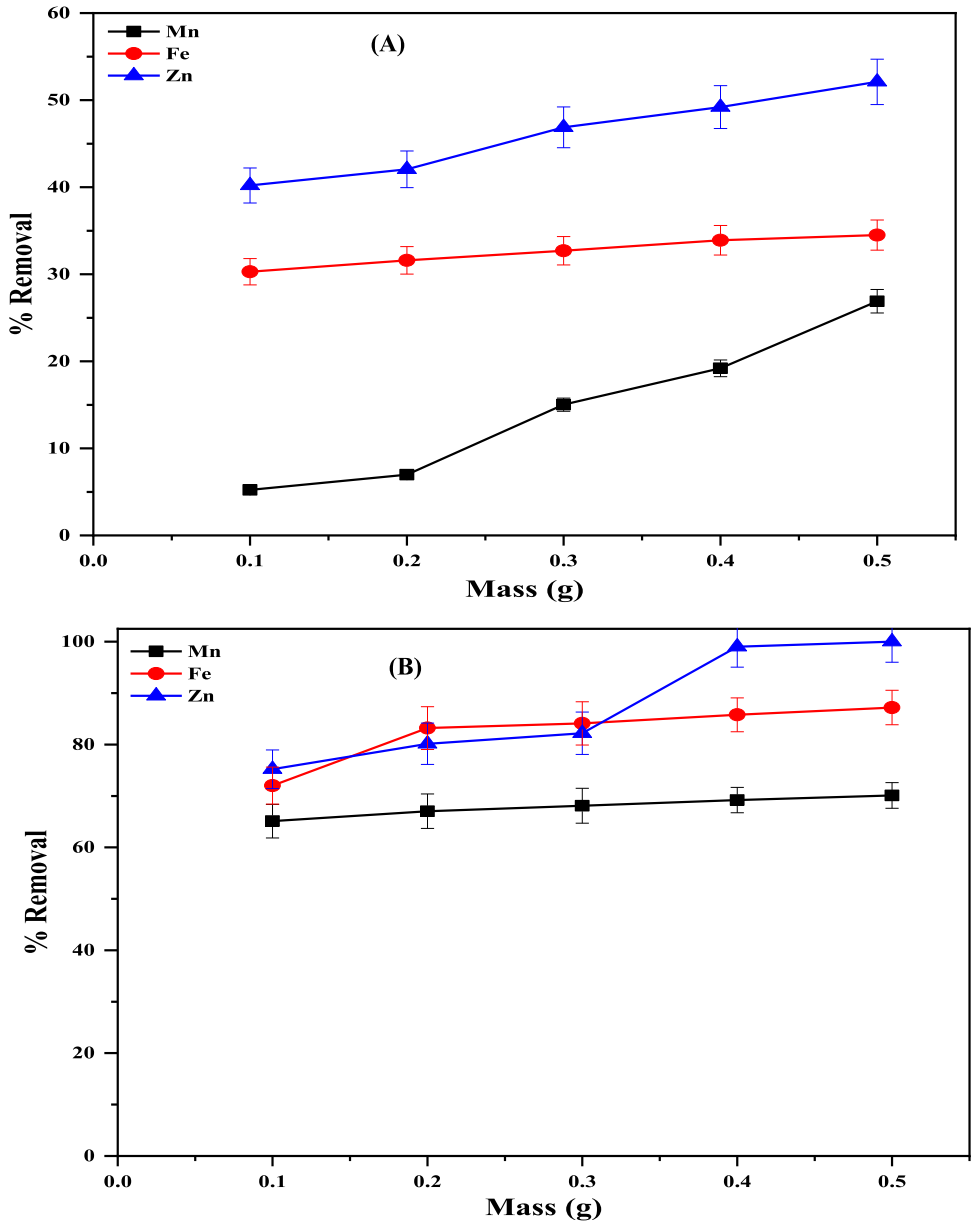

Fig. 19. Effect of dosage on heavy metals using (a) P-CNT (b) Ag-CNT (Experimental conditions: stirrer speed (120 rpm) and temperature (25 °C) volume of fish pond wastewater (50 mL), stirring time (90 min).

wastewater (see Fig. 19. According to Fig. 19(a), it can be seen that the percentage removal increases with an increasing amount of adsorbent (up to 0.5 g/L for selected metals). Of the three selected heavy metals, Zn was removed fastest, followed by Fe and Mn; the removal efficiency increased for Zn from 40.20 to 52.10% upon increasing the adsorbent from 0.1 to 0.5 g/L. Conversely, the percentage removal for Mn was low compared to the other selected heavy metals, which increased from 5.23 to 26.90%, with the maximum removal efficiency achieved under an optimum dose of 0.5 g/L.

Fig. 19(b) describes the impact of the Ag-CNTs dosage. Up until equilibrium was reached, it was discovered that the removal efficiency increased proportionally with the Ag-CNT dosage; however, once equilibrium had been reached, the removal efficiency remained constant despite the increase in Ag-CNT dosage. According to Fig. 19(b), increasing the mass of Ag-CNTs from 0.1 g to 0.3 g significantly improves the percentage adsorption of Fe, Mn, and Zn, which go from 72.01 to 84.10%, 65.15 to 68.09%, and 75.20 to 82.20%, respectively. It was found to be between 0.1 and 0.3 g for these three metals, and increasing the mass of Ag-CNTs over 0.3 g impacted the removal efficiency increase of Fe, Mn, and Zn in fish pond effluent. The removal of Fe increased from 72.01 to 87.70%, Mn from 68.10 to 70.10%, and Zn from 75.20 to 100% at the dosage of Ag-CNTs from 0.1 to 0.4 g. The availability of more adsorption sites for the metal ions adsorption may be responsible for the observed increase in removal effectiveness. The saturation of adsorption sites through the adsorption process, which leads to desorption, is the main cause of the maintenance in adsorption uptake despite the increase in adsorbent dosage (Tan et al., 2020). According to the findings in Fig. 19(a) and (b), Ag-CNTs have a higher surface area than P-CNTs, making them superior at adsorbing heavy metal ions.

Effect of temperature

The effect of temperature on the removal efficiency of the selected heavy metal ions from fish pond wastewater was carried out, and the result is shown in Fig. 20(a). It was observed that increasing the temperature from 30 to 70 °C causes an increase in the adsorption efficiency of heavy metal ions onto P-CNTs. The

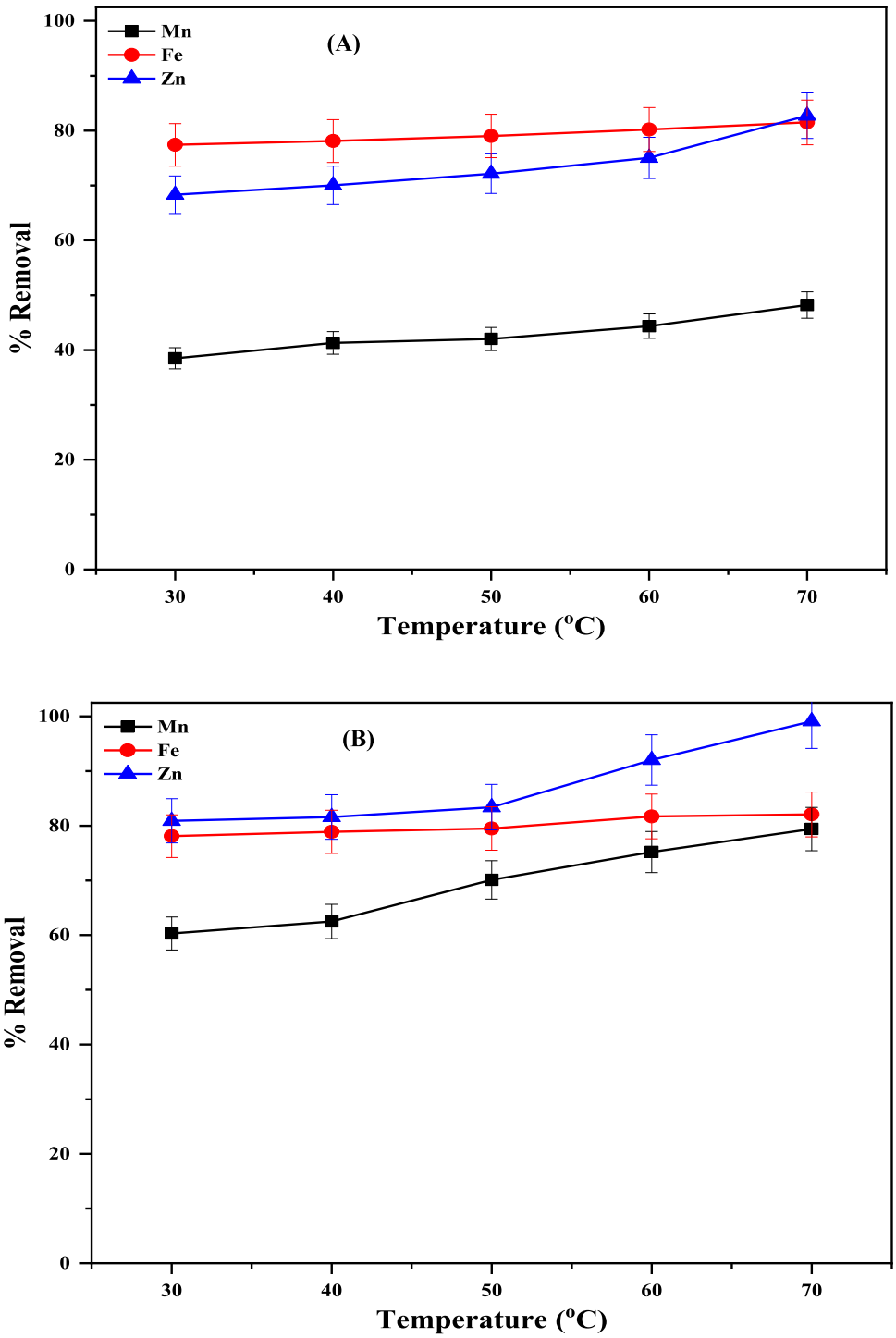

Fig. 20. Effect of temperature on heavy metals using (a) P-CNT, (b) Ag-CNT (Experimental conditions: stirrer speed (120 rpm), dosage (0.4 g), the volume of fish pond wastewater (50 mL), stirring time (90 min).

removal efficiency increased from 38.50 to 48.21% for Mn, 77.40 to 80.20% for Fe, and 68.30 to 82.72% for Zn as the temperature increased from 30 to 70 °C. This implies that the optimum temperature to achieve sufficient Mn, Zn, and Fe removal was 70 °C. Furthermore, it is possible to have significant removal efficiency of the selected heavy metals in the fish pond wastewater, increasing the temperature beyond 70 °C. Therefore, results showed that the removal of heavy metal ions using P-CNTs was potentially and comparatively favoured at high temperatures than at lower temperatures. This is because of the increased metal mobility due to temperature increment and sufficient interactions with the active sites. Moreover, an increasing temperature produces a swelling effect within the internal structure of the adsorbent, which invariably increases the rate of penetration of the active sites on the adsorbent by the metals (Hamzat et al., 2019).

Fig. 20(a) shows a similar trend to Fig. 20(b), as the temperature increased from 30 to 70 °C. The percentage removal and the adsorption capacity for the selected metals increases for the chosen temperature range. The study undertaken here is governed by the endothermic adsorption process. In the case of Mn, the removal efficiency was increased from 60.30 to 79.40%, Zn from 80.90 to 99.11%, and Fe from 78.10% to 82.07% as the

Table 8
Isotherm parameters for removing heavy metals from fish pond wastewater using purified CNTs and Ag-CNTs.

Isotherm parameter	P-CNTs			Ag-CNTs		
	Fe	Mn	Zn	Fe	Mn	Zn
Langmuir						
K_L (l/mg)	1.4478	0.3979	1.5390	8.1759	0.82473	10.1029
Q_{max} (mg/g)	0.0137	0.0053	0.0397	0.06820	0.009871	0.12177
R^2	0.4952	0.1401	0.3424	0.8967	0.8697	0.6843
Freundlich						
K_f	0.1753	6E+10	0.95120	0.1010	60.9223	0.6066
n	0.119	0.01618	0.51557	0.4329	0.0213	0.8073
R^2	0.5506	0.2821	0.8342	0.8499	0.7843	0.9274

temperature increased from 30 to 60 °C. The rate at which metal ions diffuse from the bulk of the solution to the bulk of the adsorbent rises with temperature.

Furthermore, the active adsorption sites become more active towards the adsorption from the solution as the temperature rises (Sellaoui et al., 2022). The adsorption capacity of the adsorbents at high temperatures may result from a decrease in the binding forces between the adsorbent and adsorbate caused by this temperature increase (Bankole et al., 2017). As a result of their greater surface area, availability of additional binding sites, nature of the adsorbent, and electrostatic interaction between them and the adsorbate, Ag-CNTs showed better adsorption efficiency than P-CNTs in this study.

Adsorption isotherm

The results of the adsorption process were examined using the Langmuir and Freundlich adsorption isotherm equations, as shown in Eqs. (7) and (8), to identify the isotherm parameters and model that best represent the adsorption mechanism (Table 8). The model with better applicability is determined using the adsorption regression correlation coefficient (R^2) value (Sharma et al., 2018).

$$\frac{C_e}{Q_e} = \frac{1}{K_L Q_{max}} + \frac{C_e}{Q_{max}} \tag{7}$$

$$\ln Q_e = \ln K_f + \frac{1}{n} \ln C_e \tag{8}$$

For the Fe adsorption process on P-CNTs, the values of R^2 for the Freundlich isotherm model (0.5506) are greater than those for the Langmuir model (0.4952). Similar to this, Zn and Fe are also taken up in the same trend, with R^2 values for respective Langmuir and Freundlich isotherms of 0.3424 and 0.8342 for Zn and 0.8967 and 8499 for Fe. The value of the Freundlich correlation constant (n) is another crucial factor to be considered before deciding whether the Freundlich isotherm better describes the adsorption mechanism. When the Freundlich constant n ranges in value from 1 to 10, adsorption is considered good. If n is equal to 1, the adsorption process is linear; otherwise, it is a chemical process if n is larger than 1 and a physical process if n is less than 0. For Fe, Mn, and Ze, Freundlich constant "n" values of 0.119, 0.01618, and 0.5156 are obtained.

Regarding Fe, Mn, and Zn, the values of n for Ag-CNTs were 0.4329, 0.0213, and 0.8073, respectively, and are less than 1. The R^2 values for the Freundlich isotherm with 0.8499, 0.7843, and 0.9274 for Fe, Mn, and Zn, respectively, are higher than the Langmuir model, indicating that the isotherm follows the Freundlich isotherm model. The Freundlich model presumes that multilayer adsorption takes place, according to Wang et al. (2017). This explains how the Freundlich isotherm can describe the adsorption process on MWCNTs with multiple wall layers.

Adsorption kinetic studies

Regression correlation coefficients were used in Table 9 to summarize the kinetic adsorption parameters determined from the kinetic model equations. The model that best describes the kinetics of heavy metals adsorption onto the adsorbent has a considerably higher value. In this study, the pseudo-first-order, pseudo-second-order kinetic, and Elovich models, as provided in Eqs. (9)–(11), were utilized to evaluate the adsorption kinetics (see Table 10).

$$\frac{t}{Q_t} = \frac{1}{k_2 Q_e^2} + \frac{t}{Q_e} \tag{9}$$

$$\ln (Q_e - Q_t) = \ln Q_e - k_1 t \tag{10}$$

$$Q_t = B\ln (A) + B\ln t \tag{11}$$

Table 9 shows that the pseudo-first-order model has R^2 values for Zn, Fe, and Mn of 0.0099, 0.4265, and 0.3568, respectively, for P-CNTs. This indicates that the pseudo-first-order model is unsuitable for fitting the adsorption process since the values of R^2 are not close to 1. The pseudo-first-order model does not accurately describe the kinetic adsorption process for Ag-CNTs, as shown by the R^2 values of 0.0078, 0.6373, and 0.6924 for Zn, Fe, and Mn, respectively. The calculated pseudo-second-order parameters, however, exhibit greater correlation values. When the Ag-CNTs adsorbent was utilized, the R^2 values for Zn, Fe, and Mn were 0.9999, 0.9869, and 0.9101, respectively, and R^2 values of 0.9992, 0.9987, and 0.9927 were obtained for Zn, Fe, and Mn, respectively, for the P-CNTs. Because the values are close to 1, this also displays the best fit. Additionally, the R^2 values for Zn, Fe, and Mn for P-CNTs in the Elovich model are 0.8279, 0.9523, and 0.8632, respectively. The values of R^2 for Zn, Fe, and Mn when employing the Ag-CNTs are 0.8952, 0.6484, and 0.8582, respectively. This suggests that the Elovich model is likewise acceptable for fitting the adsorption process because the values of R^2 are also close to 1. As can be seen, the pseudo-second-order kinetic model has a higher R^2 value than the Elovich and pseudo-first-order kinetic models. The fitness of kinetic models for the adsorption of Mn, Zn, and Fe from the wastewater of fish ponds by nanoadsorbents followed the pattern; pseudo-second-order kinetic > Elovich model > pseudo-first-order kinetic. With respect to the FTIR and textural properties of the adsorbents, ion exchange and surface complexation could be responsible for the adsorption process via the combination of the positively charged metal ions and the active-sited negatively charged groups of the adsorbents. This phenomenon occurs through the attraction of metal ions to the surface of the adsorbents.

Thermodynamic studies

The change in Gibbs free energy (ΔG) was established to understand the spontaneity of the adsorption process to study adsorption thermodynamics. Tables 11 and 12 show that thermodynamic study variables such as a change in enthalpy (ΔH) and change in entropy (ΔS) were calculated for purified and functionalized CNTs. The slopes from the plots of lnKd against 1/T were used to calculate the ΔH values. The ΔS (J/mol K) was determined using the Gibbs–Helmholtz equation.

The temperature range (303 to 343 K) was used for adsorption based on the ΔG values in Tables 11 and 12. The heavy metals

Table 9
Kinetic parameters for the adsorption of selected heavy metals on P-CNTs and Ag-CNTs.

Kinetic parameters	P-CNTs			Ag-CNTs		
	Zn	Fe	Mn	Zn	Fe	Mn
Pseudo-first-order						
k_1 (min)	0.0025	0.0228	0.0277	0.0022	0.012	0.0338
$Q_{e\ exp}$ (mg/g)	6.595	15.30	11.17	6.59	16.60	19.76
Q_{ecal} (mg/g)	0.3575	3.6677	3.661	0.1347	4.2599	18.9714
R^2	0.0099	0.4265	0.3568	0.0078	0.6373	0.6924
Pseudo-second-order						
k_2 (g/mg.min)	0.0490	0.0078	0.0073	0.0062	0.0062	0.0008
Q_e (mg/g)	6.7024	16.3132	12.4378	6.6533	1.3310	27.5482
R^2	0.9992	0.9987	0.9927	0.9999	0.9869	0.9101
Elovich						
B	4.1305	0.5288	0.5421	7.6103	0.7224	0.1587
A	1E+09	57.6126	8.3197	5.74E18	1087.037	1.3550
R^2	0.8279	0.9523	0.8632	0.8952	0.6484	0.8582

Table 10
Comparison of the adsorption capacity for Mn and Fe ions removal with previous literature.

Adsorbent	Wastewater	Surface area (m^2/g)	Adsorption capacity (mg/g)	Reference
Diethylenetriamine/CNTs/GO	Synthetic		Fe^{3+} = 13.80 Mn^{2+} = 9.50	Zhu et al. (2016b)
Cashew nut shell	Electroplating	608.20	Mn^{2+} = 9.82	Yahya et al. (2020)
Activated carbon	Industrial	688.60	Fe^{3+} = 14.86 Mn^{2+} = 7.63	Goher et al. (2015)
MWCNTs	Acid mine drainage	105.54	Mn^{2+} = 7.63	Rodríguez and Leiva (2019)
MWCNTs	Synthetic	157.34	Mn^{2+} = 7.63	Rodríguez et al. (2020)
P-CNTs	Fish pond	268.40	Fe^{3+} = 16.31 Mn^{2+} = 12.44	This study
Ag-CNTs	Fish pond	1068	Fe^{3+} = 1.33 Mn^{2+} = 27.55	This study

Table 11
Thermodynamic parameters of the selected heavy metals adsorption using P-CNTs.

Heavy metal	T (K)	ΔH (kJmol^{-1})	ΔS (kJmol^{-1}K^{-1})	ΔG (kJmol^{-1})
Mn	303	−1.05	1.36	−1.46
	313			−1.47
	323			−1.49
	333			−1.50
	343			−1.51
Fe	303	−1.36	5.47	−3.02
	313			−3.07
	323			−3.13
	333			−3.18
	343			−3.24
Zn	303	−3.48	6.29	−5.38
	313			−5.45
	323			−5.51
	333			−5.57
	343			−5.63

spontaneously adsorb on pure CNTs, as seen by the negative values of ΔG, indicating that the process will continue at these temperatures. The negative values ΔG obtained could increase as the temperature increases. This demonstrates how an increase in temperature promotes the adsorption spontaneity. The increase in randomness at the sorbate–solution interface during the adsorption process is indicated by the positive values of change in entropy. A negative ΔG value indicates a favourable reaction. The adsorption is more advantageous as the temperature rises, as indicated by an increase in the value of ΔG. Additionally, the increase in randomness at the solid/liquid interface throughout the adsorption process and enhanced Ag-CNT adsorption for the chosen heavy metals were indicated by the positive value of ΔS.

Regeneration study

Fig. 21(a) and (b) show the removal of Fe, Zn, and Mn from fish and wastewater and the efficacy and durability of purified CNTs and Ag-CNTs as reusable nanoadsorbents. After the nanoadsorbents were synthesized and utilized for the first adsorption process, they were retained and reused up to 5 times using HNO_3 as a reagent for desorbing contaminants from the nanoadsorbents. From Fig. 21(a), it has been proved that regeneration did not negatively affect the adsorption of heavy metals onto the Ag-CNTs during 5 cycles, indicating that the nanoadsorbent has a high level of stability. However, the adsorption of the metal ions onto purified CNTs during 5 cycles of regeneration drops through 3 cycles (see Fig. 21b). Therefore, it can be concluded that the decoration of CNTs with AgNPs performed better in the

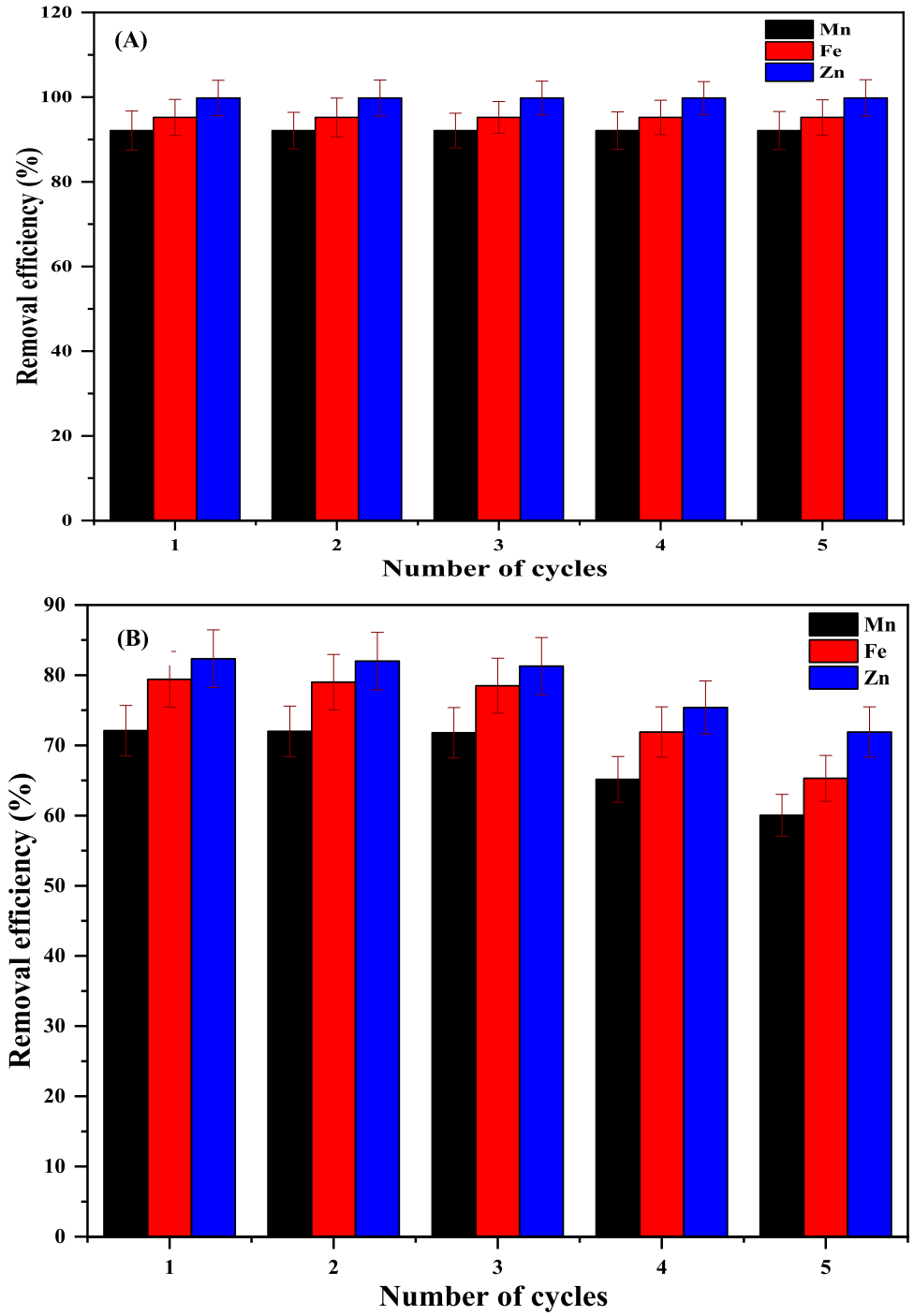

Fig. 21. Stability of (a) A-CNTs and (b) P-CNTs for removal of Mn, Fe, and Zn.

adsorption process under regeneration study for the adsorption of metal ions.

5. Conclusion

In this study, Ag-doped MWCNTs are synthesized to remediate fishpond effluent. Silver nanoparticles were synthesized using *Carica papaya* leaf extract via the green synthesis technique. Using this plant as a reducing and stabilizing agent is demonstrated by the synthesized AgNPs. The presence of elemental silver was confirmed by UV-visible spectroscopy, HRTEM, and XRD. The surface plasmon resonance peak, 419.50 nm, is associated with silver nanoparticles, and the particle size of as-synthesized AgNPs was estimated to be between 11.12 and 15.39 nm. The CCVD method was used to prepare the bimetallic catalyst on kaolin support Fe–Ni/kaolin; the catalyst preparation is suitable for the production of CNTs at the experimental conditions of 8 g mass of support, oven drying temperature of 140 °C, oven drying time of 8 h, and a stirring speed of 240 rpm. Ag nanoparticles were doped on the surface of pure carbon nanotubes by the wet impregnation method. The FTIR confirmed the formation of Ag-CNTs, and the HRTEM showed that the well-dispersed and spherical Ag nanoparticles were anchored on the MWCNTs. The contact time, adsorbent dosage, and temperature influenced the efficiency of P-CNTs and Ag-CNTs in removing Fe, Mn, and Zn metals from fish pond effluent. Ag-CNTs were more effective in

Table 12
Thermodynamic parameters of the selected heavy metals adsorption using Ag-CNTs.

Heavy metal	T (K)	ΔH (kJmol^{-1})	ΔS (kJmol^{-1}K^{-1})	ΔG (kJmol^{-1})
Mn	303	−1.48	3.57	−2.56
	313			−2.60
	323			−2.63
	333			−2.67
	343			−2.70
Fe	303	−0.34	15.15	−4.93
	313			−5.08
	323			−5.23
	333			−5.38
	343			−5.53
Zn	303	−5.09	13.83	−9.28
	313			−9.42
	323			−9.56
	333			−9.70
	343			−9.83

removing the selected heavy metals than P-CNTs. The Freundlich isotherm and the pseudo-second-order model were best matched to the adsorption isotherm and the kinetic model, respectively, demonstrating that it is a multilayer phenomenon. Fe, Zn, and Mn adsorption processes from fish pond wastewater were random, feasible, and spontaneous. This study demonstrated that Ag-CNTs are more promising nanoadsorbents for the adsorption of heavy metals from fish pond effluent than purified CNTs. However, it is of great relevance to study the microbial activities of the wastewater before and after treatment over a lengthy period and the possibility of reusing the treated polluted wastewater for other applications such as household activities.

CRediT authorship contribution statement

Saadatu Aliyu: Investigation, Writing – original draft, Writing – review & editing. **Abdulkareem Saka Ambali:** Project administration, Resources, Supervision, Validation, Visualization, Writing – review & editing. **Tijani Jimoh Oladejo:** Project administration, Resources, Supervision, Validation, Visualization, Writing – review & editing. **Saheed Mustapha:** Conceptualization, Validation, Writing – original draft, Writing – review & editing. **Titus Chinedu Egbosiuba:** Validation, Writing – original draft, Writing – review & editing. **Samson Oluwaseyi Bada:** Validation, Writing – original draft, Writing – review & editing.

Declaration of competing interest

The authors declare that they have no known competing financial interests or personal relationships that could have appeared to influence the work reported in this paper.

Data availability

Data will be made available on request.

Acknowledgements

The authors are grateful to the contributions of Dr. Remy iBucher (XRD analysis, I Temba Lab, South Africa) and Dr. Franscious Cummings (HRSEM/EDX and HRTEM/SAED analysis, Physics Department, University of the Western Cape, South Africa) for their technical support. This work was supported by the Tertiary Education Trust Fund (TETFund) of Nigeria under grant number TETFUND/FUTMINNA/2019/B7/16

References

Alfarisa, S., Safitri, R., Dwandaru, W., 2016. Effect of catalyst concentrations on the growth of carbon nanotubes from waste engine oil. EDUCATUM J. Sci. Math. Technol. 3 (1), 6–12.
Aliyu, A., Abdulkareem, A., Kovo, A., Abubakre, O., Tijani, J., Kariim, I., 2017a. Synthesize multi-walled carbon nanotubes via catalytic chemical vapour deposition method on Fe-Ni bimetallic catalyst supported on kaolin. Carbon Lett. 21, 33–50.
Aliyu, A., Kariim, I., Abdulkareem, S.A., 2017b. Effects of aspect ratio of multi-walled carbon nanotubes on coal washery wastewater treatment. J. Environ. Manag. 202, 84–93.
Amendola, V., Pilot, R., Frasconi, M., Maragò, O.M., Iatì, M.A., 2017. Surface plasmon resonance in gold nanoparticles: a review. J. Phys.: Condens. Matter 29 (20), 203002.
American Public Health Association (APHA), 2017. Standard Methods for the Examination of Water and Wastewater, 23rd ed. APHA American Public Health Association, Washington, D.C..
Anijiofor, S.C., Daud, N.N.N., Idrus, S., Man, H.C., 2018. Recycling of fishpond wastewater by adsorption of pollutants using aged refuse as an alternative low-cost adsorbent. Sustain. Environ. Res. 28 (6), 315–321.
Anon, 2009. National Environmental Standards and Regulations Enforcement Agency (Establishment). NESREA, S.I. No. 28 of 2009.
Bamisaye, F.A., Ajani, E.O., Minari, J.B., 2013. Prospects of ethnobotanical uses of pawpaw (*Carica papaya*). J. Med. Plants 1 (4), 171–177.
Bankole, M., Abdulkareem, A., Tijani, J., Ochigbo, S., Afolabi, A., Roos, W., 2017. Chemical oxygen demand removal from electroplating wastewater by purified and polymer functionalized carbon nanotubes adsorbents. Water Res. Ind. 18, 33–50.
Burakova, E.A., Dyachkova, T.P., Rukhov, A.V., Tugolukov, E.N., Galunin, E.V., Tkachev, A.G., Ali, I., 2018. Novel and economic method of carbon nanotubes synthesis on a nickel magnesium oxide catalyst using microwave radiation. J. Molecular Liq. 253, 340–346.
Chandhru, M., Logesh, R., Rani, S.K., Ahmed, N., Vasimalai, N., 2019. One-pot green route synthesis of silver nanoparticles from jack fruit seeds and their antibacterial activities with escherichia coli and salmonella bacteria. Biocatal. Agric. Biotechnol. 20, 101241.
Cuong, D.V., Wu, P.C., Liu, N.L., Hou, C.H., 2020. Hierarchical porous carbon derived from activated biochar as an eco-friendly electrode for the electrosorption of inorganic ions. Sep. Purif. Technol. 242, 116813.
Dey, S., Dhal, G.C., 2019. Applications of silver nanocatalysts for low-temperature oxidation of carbon monoxide. Inorganic Chem. Comm. 110, 107614.
Farid, M., Ali, S., Zubair, M., Saeed, R., Rizwan, M., Sallah-Ud-Din, R., Azam, A., Ashraf, W., 2018. Glutamic acid assisted phyto-management of silver-contaminated soils through sunflower; physiological and biochemical response. Environ. Sci. Pollut. Res. 25 (25), 25390–25400.
Goher, M.E., Hassan, A.M., Abdel-Moniem, I.A., Fahmy, A.H., Abdo, M.H., El-sayed, S.M., 2015. Removal of aluminum, iron and manganese ions from industrial wastes using granular activated carbon and Amberlite IR-120H. Egypt. J. Aquat. Res. 41 (2), 155–164.
Goscianska, J., Pietrzak, R., 2015. Removal of tartrazine from aqueous solution by carbon nanotubes decorated with silver nanoparticles. Catalysis Today 249, 259–264.
Gunjakar, J., More, A., Gurav, K., Lokhande, C., 2008. Chemical synthesis of spinel nickel ferrite ($NiFe_2O_4$) nano-sheets. Appl. Surf. Sci. 254 (18), 5844–5848.
Hamzat, W.A., Abdulkareem, A.S., Bankole, M.T., Tijani, J.O., Kovo, A.S., Abubakre, O.K., 2019. Adsorption studies on the treatment of battery wastewater by purified carbon nanotubes (P-CNTs) and polyethylene glycol carbon nanotubes (PEG-CNTs). J. Environ. Sci. Health Part A 54 (9), 827–839.

Karim, M.N., Anderson, S.R., Singh, S., Ramanathan, R., Bansal, V., 2018. Nanostructured silver fabric as a free-standing NanoZyme for colorimetric detection of glucose in urine. Biosens. Bioelectron. 110, 8–15.
Khalatbary, M., Sayadi, M.H., Hajiani, M., Nowrouzi, M., Homaeigohar, S., 2022. Green, sustainable synthesis of γ-Fe_2O_3/MWCNT/Ag nano-composites using the viscum album leaf extract and waste car tire for removal of sulfamethazine and bacteria from wastewater streams. Nanomaterials 12 (16), 2798.
Li, L., Hu, Y., Ling, L., 2016. Wave propagation in viscoelastic single-walled carbon nanotubes with surface effect under magnetic field based on nonlocal strain gradient theory. Phys. E 75, 118–124.
Lokhande, R.S., Singare, P.U., Pimple, D.S., 2011. Toxicity study of heavy metals pollutants in waste water effluent samples collected from Taloja industrial estate of Mumbai, India. Res. Environ. 1 (1), 13–19.
Lu, L., Sun, R., Chen, R., Hui, C.K., Ho, C.M., Luk, J.M., Lau, G., Che, C.M., 2008. Silver nanoparticles inhibit hepatitis B virus replication. Antiviral Therapy 13 (2), 253.
Luo, J., Im, J.M., Mayer, M.T., Schreier, M., Nazeeruddin, M.K., Park, N.G., Tilley, S.D., Fan, H.J., Grätzel, M., 2014. Water photolysis at 12.3% efficiency via perovskite photovoltaics and earth-abundant catalysts. Sci. 345 (6204), 1593–1596.
Mamudu, A., Emetere, M., Okocha, D., Taiwo, S., Ishola, F., Elehinafe, F., Okoro, E., 2020. Parametric investigation of indigenous Nigeria mineral clay (Kaolin and Bentonite) as a filler in the Fluid Catalytic Cracking Unit (FCCU) of a petroleum refinery. Alexandria Engineering Journal 59 (6), 5207–5217.
Mohanta, Y.K., Panda, S.K., Jayabalan, R., Sharma, N., Bastia, A.K., Mohanta, T.K., 2017. Antimicrobial, antioxidant and cytotoxic activity of silver nanoparticles synthesized by leaf extract of Erythrina suberosa (Roxb.). Front. Molecul. Biosci. 4 (14).
Montazer, M., Alimohammadi, F., Shamei, A., Rahimi, M.K., 2012. In situ synthesis of nano silver on cotton using Tollens' reagent. Carbohyd. Polymers 87 (2), 1706–1712.
Mustapha, S., Ndamitso, M.M., Abdulkareem, A.S., Tijani, J.O., Mohammed, A.K., Shuaib, D.T., 2019. Potential of using kaolin as a natural adsorbent for the removal of pollutants from tannery wastewater. Heliyon 5 (11), e02923.
Omitoyin, B., Ajani, E., Okeleye, O., Akpoilih, B., Ogunjobi, A., 2017. Biological treatments of fish farm effluent and its reuse in the culture of Nile Tilapia (Oreochromis niloticus). J. Aquacult. Res. Dev. 8 (2).
Oni, S.K., Futter, M.N., Bishop, K., Köhler, S., Ottosson-Löfvenius, M., Laudon, H., 2013. Long-term patterns in dissolved organic carbon, major elements and trace metals in boreal headwater catchments: trends, mechanisms and heterogeneity. Biogeosci 10 (4), 2315–2330.
Rahmanian, N., Ali, S.H.B., Homayoonfard, M., Ali, N., Rehan, M., Sadef, Y., Nizami, A., 2015. Analysis of physiochemical parameters to evaluate the drinking water quality in the state of Perak. Malaysia. J. Chem. 2015.
Rodríguez, C., Briano, S., Leiva, E., 2020. Increased adsorption of heavy metal ions in multi-walled carbon nanotubes with improved dispersion stability. Molecules 25 (14), 3106.
Rodríguez, C., Leiva, E., 2019. Enhanced heavy metal removal from acid mine drainage wastewater using double-oxidized multiwalled carbon nanotubes. Molecules 25 (1), 111.
Sagadevan, S., Vennila, S., Marlinda, A.R., Al-Douri, Y., Johan, M.R., Lett, J.T., 2019. Synthesis and evaluation of the structural, optical, and antibacterial properties of copper oxide nanoparticles. Appl. Phys. A 125 (8), 1–9.
Salahudeen, N., 2018. Metakaolinization effect on the thermal and physiochemical propperties of kankara kaolin. Applied Science and Engineering Progress 11 (2), 127–135.
Sellaoui, L., Dhaouadi, F., Taamalli, S., AlZahrani, H.Y.S., Louis, F., Bakali, A.E., Erto, A., Lamine, A.B., Lima, D.R., Lima, E.C., Chen, Z., 2022. Application of a multilayer physical model for the critical analysis of the adsorption of nicotinamide and propranolol on magnetic-activated carbon. Environ. Sci. Pollut. Res. 29 (20), 30184–30192.
Sharma, J., Kaith, B.S., Sharma, A.K., Goel, A., 2018. Gum xanthan-psyllium-cl-poly (acrylic acid-co-itaconic acid) based adsorbent for effective removal of cationic and anionic dyes: adsorption isotherms, kinetics and thermodynamic studies. Ecotoxicol. Environ. Safety 49, 150–158.
Tan, T.L., Nakajima, H., Rashid, S.A., 2020. Adsorptive, kinetics and regeneration studies of fluoride removal from water using zirconium-based metal organic frameworks. RSC Adv. 10 (32), 18740–18752.
Tan, Y., Sun, L., Wang, G., Zhang, R., Hou, J., Zhang, R., Zhao, W., 2022. A two-step nonthermal plasma method to fabricate Ag/N-doped TiO_2/CNTs for formaldehyde removal under visible light irradiation. J. Clean. Prod. 370, 133507.
Teh, C.Y., Budiman, P.M., Shak, K.P.Y., Wu, T.W., 2016. Recent advancement of coagulation–flocculation and its application in wastewater treatment. Indust. Eng. Chem. Res. 55 (16), 4363–4389.
Verma, P., Maheshwari, S.K., 2019. Applications of silver nanoparticles in diverse sectors. Inter. J. Nano Dimen. 10 (1), 18–36.
Wang, L., Qiang, Z., Li, Y., Ben, W., 2017. An insight into the removal of fluoroquinolones in activated sludge process: Sorption and biodegradation characteristics. J. Environ. Sci. 56, 263–271.
World Health Organization (WHO), 2015. Progress on Sanitation and Drinking-Water: Fact Sheet No. 391.
Yahya, M.D., Aliyu, A.S., Obayomi, K.S., Olugbenga, A.G., Abdullahi, U.B., 2020. Column adsorption study for the removal of chromium and manganese ions from electroplating wastewater using cashew nutshell adsorbent. Cogent Eng. 7 (1), 1748470.
Yang, Y., Liu, K., Sun, F., Liu, Y., Chen, J., 2022. Enhanced performance of photocatalytic treatment of Congo red wastewater by CNTs-Ag-modified TiO_2 under visible light. Environ. Sci. Pollut. Res. 29 (11), 15516–15525.
Zargar, M., Shameli, K., Najafi, G.R., Farahani, F., 2014. Plant mediated green biosynthesis of silver nanoparticles using vitex negundo L. extract. J. Indust. Eng. Chem. 20 (6), 4169–4175.
Zhu, X., Cui, Y., Chang, X., Wang, H., 2016a. Selective solid-phase extraction and analysis of trace-level Cr(III), Fe(III), Pb(II), and Mn(II) Ions in wastewater using diethylenetriamine-functionalized carbon nanotubes dispersed in graphene oxide colloids. Talanta 146, 358–363.
Zhu, B., Li, Y., Lin, Z., Zhao, M., Xu, T., Wang, C., Deng, N., 2016b. Silver nanoparticles induce HePG-2 cells apoptosis through ROS-mediated signaling pathways. Nanoscale Res. Lett. 11 (1), 1–8.